Department of Physics and Astronomy

University of Heidelberg

Master thesis

in Physics

submitted by

Pablo Herrero Gómez

born in Teruel, Spain

2018

Investigation of surface cleaning procedures for the removal of radon daughters from PTFE surfaces and their applicability in liquid xenon detectors.

This Master thesis has been carried out by Pablo Herrero Gómez

at the

Max Planck Institut für Kernphysik

under the supervision of

Herrn Prof. Manfred Lindner

Untersuchung von Oberflächenreinigungsverfahren zur Entfernung von Radon-Nachkommen aus PTFE-Oberflächen und deren Anwendbarkeit in flüssigen Xenon-Detektoren.:

Die Identifizierung und Reduktion von Untergrundsignalen ist für Experimente mit geringen Ereignisraten von aussenordentlicher Wichtigkeit. Das gilt auch für das XENON1T Dunkle Materie Experiment wo das radioaktive Edelgas Radon und insbesondere dessen Zerfallstöchter die dominanten Untergrundquellen darstellen. Radontöchter können sich aus der Luft auf der Oberfläche auf allen Detektormaterialien und besonders auf PTFE absetzen. Dieses Polymer wird zur Begrenzung des Detektors verwendet und steht daher in direktem Kontakt zum sensitiven Targetmaterial des Detektors. In dieser Arbeit werden verschiedene Oberflächenreinigungsverfahren zur Entfernung von radioaktiven Verunreinigungen von PTFE entwickelt. Mit einem eigens entwickelten Versuchsaufbau wird die Reinigungseffizienz und die Anwendbarkeit der Prozeduren im zukünftigen XENONnT Detektor untersucht.

Investigation of surface cleaning procedures for the removal of radon daughters from PTFE surfaces and their applicability in liquid xenon detectors:

Background identification and suppression is of paramount importance for experiments seeking extremely rare events. Direct dark matter searches such as the XENON1T experiment fall in this category. ^{222}Rn daughters are the dominant contribution to the internal background of the XENON1T detector. Air contains traces of radon which plates out its progeny onto the surface of the detector materials, such as the PTFE. This polymer is in direct contact with the sensitive liquid xenon as it is used to house the detector's dual-phase time projection chamber. The effects of surface cleaning procedures to remove surface sources from PTFE are investigated in this work. With a dedicated experimental setup, we investigate the efficiency of standard surface treatments and their applicability for XENON1T and the future upgrade XENONnT.

Contents

1 Dark Matter Searches with XENON

The existence and nature of dark matter constitutes one of the most puzzling enigmas in contemporary cosmology and particle physics. Having to account for 25.6% of the total energy content of the universe [1] and postulated as non-baryonic, non-luminous matter, it falls out of the framework of the Standard Model of Particle Physics. Nevertheless, its gravitational interaction with photons and baryonic matter entails the possibility for astrophysicists to trace its abundance and model its distribution in the cosmos.

One of the most encouraging candidates to meet the features dark matter exhibits is the so-called Weakly Interacting Massive Particle (WIMP). A whole number of experiments targeting to detect this hypothetical particle have arisen in the last decades. Direct detection of such particles would provide a measure of the particle's mass and cross-section for its interaction with the detector's target nuclei. It would also set a positive prove of the ΛCDM cosmological model. The XENON experiments seek direct detection of WIMPs and embodies the framework of this study.

1.1 Dark matter detection

Back in 1933, F. Zwicky suggested for the first time the presence of "[...] *an enormous density of dark matter*" to explain the unexpectedly high dispersion velocities of individual nebulae in the Coma cluster [2]. By 1970, Rubin and Ford [3] researched the dependence of rotational velocities v of the stars in Andromeda on their distance r to the center of the galaxy. They found this relation to be in contradiction with Keplerian prediction, $v \propto r^{-1/2}$, at large distances, where the so-called "rotation curves" reach a plateau. The same effect appears in our own and other galaxies [4]. To reconcile these observations with theory, astrophysicists put forth the concept of a homogeneous *dark matter halo* braided with the luminous matter in the galaxies.

Such halos can be spotted by gravitational lensing. In the context of general relativity, a large gravitational potential deflects the light coming from distant sources as it follows the geodesic line to an observer. The mass of the object causing this bending is directly proportional to the deflection angle, allowing for a mapping of the gravitational potential [6]. In this fashion, the renamed 'Bullet Cluster' provides a striking indication of the existence of dark matter [5]. Figure 1.1 shows clear displacements of the gravitational contours (green) nuclei from the luminous mass (colored gradient). Gravitational lensing dictates the reconstruction of the green curves in the figure, whereas the intracluster plasma, conforming most of the baryonic matter, is visible in X-rays.

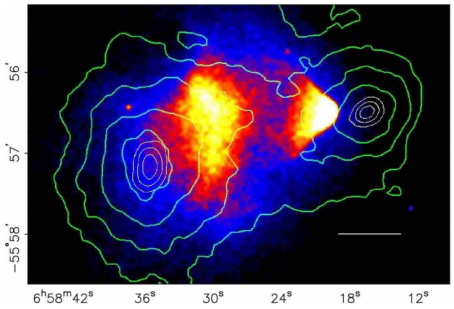

Figure 1.1: Weak lensing reconstruction of the Bullet Cluster potential (green curves) overlapping the Chandra X-ray emissions corresponding to the baryonic contribution. Figure extracted from [5].

This distribution is the result of a collision of two subclusters where the plasma is dragged down by ram pressure, while dark matter crosses unaffectedly. Limits on the cross-section of self-interacting dark matter (SIDM) can be set from the offset between the dark matter and gas centroids [7].

The content of dark matter in the universe is inferred from the fit of *Planck* data [1] of the temperature anisotropies in the cosmic microwave background (CBM) to the ΛCDM model. This parametrization of the anisotropies' power spectrum results into the following relative abundances: 4% baryonic matter, 27% dark matter and 69% dark energy.

Several properties of the standard dark matter particle can be summarized at this point: it is massive (interacts through gravity), it must not interact via electromagnetic force nor strong interaction (neutral particle) and it can couple to the electroweak gauge bosons. This rules out all known particles in the Standard Model except neutrinos. Additionally, it needs to be stable over cosmological timescales to account for its observed effects in the early Universe. Furthermore, the role it plays in the structure formation of the universe constrains its thermal velocity to be non-relativistic [8]. Thus, neutrinos drop out as candidates too.

Dark matter particles must be sought in the language of physics beyond the Standard Model (BSM). A promising candidate fulfilling the aforementioned requisites is the Weakly Interacting Massive Particle (WIMP). The so-called "*WIMP miracle*" strongly supports its candidature. This is the name given to the agreement of the relic dark matter density as predicted by WIMP models with that inferred from the observed density [9]. This prediction considers an annihilation cross-section in the range of the weak interaction coupling and masses in the scale of GeV - TeV, consistent with the assumption of the dark matter particle as weak-interacting.

The term WIMP encompasses a class of particles which stem from different BSM theories. The Minimal Supersymmetric Standard Model (MSSM) predicts four Majorana fermions, the neutralinos, among which the lightest of them (LNP) would be a WIMP candidate. In modern Kaluza-Klein models, the lightest of the infinitely many partners of the hypercharge gauge boson, B^1, also falls in the WIMP category. Other proposed candidates for dark matter particle are the lighter axions and axion-like particles (ALP), the gravitino in MSSM and sterile neutrinos. For further details on the existing dark matter candidates, the reader is referred to [9].

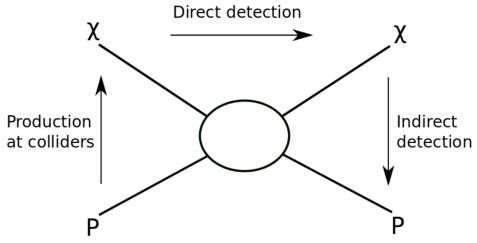

Figure 1.2: Possible modes of dark matter (χ) interactions with Standard Model particles (P) and the corresponding detection strategies. Figure published in [10].

The three conventional channels of dark matter detection are sketched in figure 1.2. The signature of dark matter production via collision of standard model particles (PP $\rightarrow \chi\chi$) is probed as missing energy in the event reconstruction. However, this approach lacks the capability of proving the stability of the dark matter particle. For recent reviews of the searches carried out in the Large Hadron Collider (LHC) we refer to [11] and [12]. Indirect-detection-oriented experiments seek for dark mat-

ter possible self-annihilation and decay products in regions of the space where the particle flux would exceed the expectation. These experiments focus on different products, e.g. IceCube measures solar neutrinos [13], H.E.S.S. on γ-rays [14] and PAMELA on positrons and anti-protons [15].

In the following we concentrate on direct detection as it provides the context of this work. This method explores the scattering of a WIMP off the target material of an Earth-based detector as it moves through the galactic dark matter halo. A discovery through this channel would provide solid evidence of the existence of dark matter independent of the precise coupling mechanism. The expected interaction is so rare that only single nuclear collisions can be considered sensible signals. Thus, multiple scattering events are neglected. The differential rate for WIMP-nuclei events per recoil energy E can be written as [16]:

$$\frac{\mathrm{d}R}{\mathrm{d}E}(E,t) = N_T \frac{\rho_\chi}{m_\chi} \int_{v_{\min}}^{v_{\mathrm{esc}}} \frac{\mathrm{d}\sigma(v,E)}{\mathrm{d}E}\ f(v,t)\ v\ \mathrm{d}v. \tag{1.1}$$

Two astrophysical parameters appear in equation (1.1): the local dark matter density at our position in the galaxy ρ_χ, which takes an approximate value of 0.3 GeV [17] and $f(v,t)$, the WIMP velocity distribution in the halo. The latter is modeled as an isotropic Maxwell-Boltzmann distribution [18] and introduces the two limits of the integral: $v_{\min}$, the minimal velocity at which the WIMP can cause a back-scattering, and v_{esc}, the Milky Way escape velocity. The detector size enters into the equation in terms of the number of target nuclei N_T and it is directly proportional to the event rate. The WIMP mass is denoted by m_χ and depends on the particle model. Finally, the differential WIMP-nucleus scattering cross-section, $\mathrm{d}\sigma/\mathrm{d}E$ can be decomposed in a spin-dependent (SD) and spin-independent (SI) part. The former scales with the nuclear total spin J as $(J+1)/J$, while the latter scales with the nuclear number of the target atom A, as A^2, if one assumes isospin conserving interaction [10]. This favors heavy nuclei as target material in the spin-independent searches. Hence, many leading experiments use such materials to maximize the expected event rate. So is the case of the XENON experiments, featuring a two-phase liquid xenon time projection chamber (TPC).

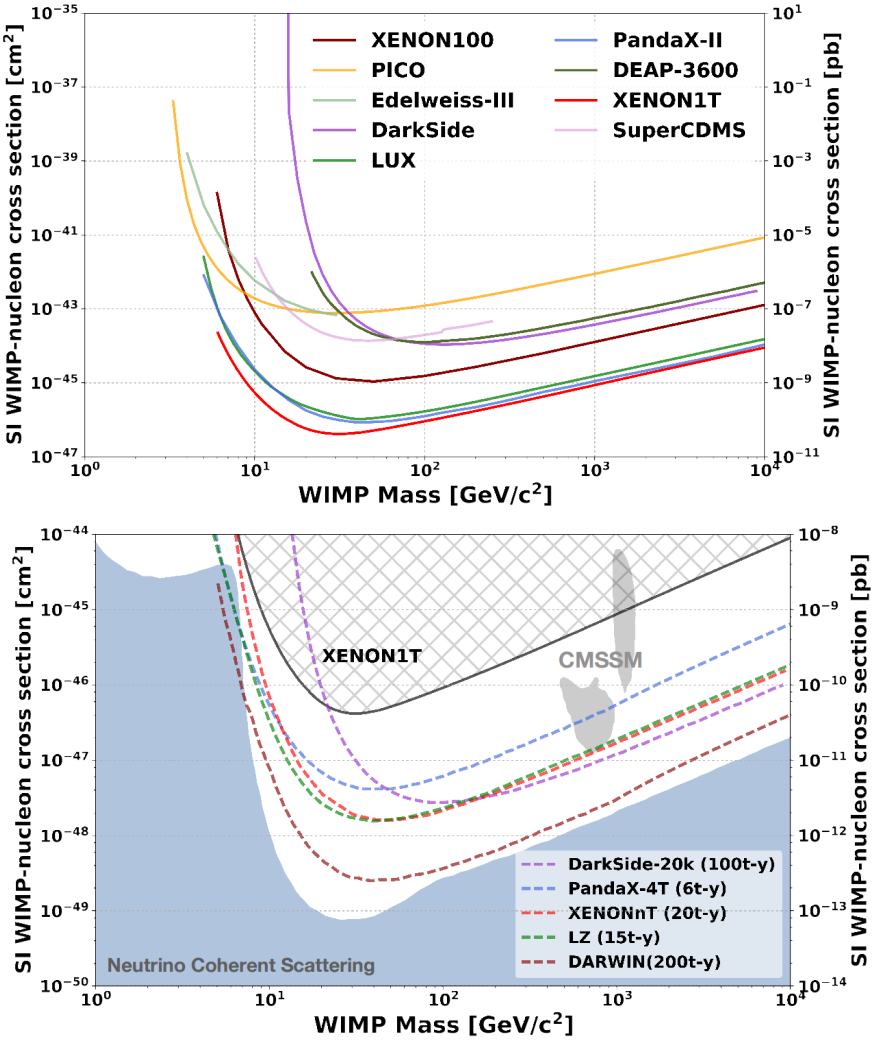

Figure 1.3: Top: Current exclusion limits on the spin-independent WIMP-nucleon cross-section published by various direct detection experiments. Bottom: In dashed lines, expected sensitivities of the next-generation experiments compared to the best limit placed by the recent XENON1T 1t·yr exposure, in solid black line.

If the measured event rate surpasses the background, a signal can be claimed with a certain significance. On the other side, a recorded rate compatible with the background permits the placing of exclusion limits. Such limits probe the parameter space of WIMP mass and WIMP-nucleon interaction cross-section. In figure 1.3 the most recent limits for spin-independent interaction are shown (top). The predicted future sensitivities of the next-generation upgrades are shown in the bottom figure too, including the regions favored by the constrained MSSM and the coherent neutrino scattering detection floor [19]. For WIMP masses above 6 GeV/c^2, the XENON1T experiment reports the most stringent cross-section with an upper limit of 4.1 $\times$ 10^{-47} cm^2 at a mass of 30

GeV/c^2 [20]. This result improves by a factor ≈ 7 the previous dark matter best limits. Following closely, the LUX and PandaX-II experiments [21][22] employ liquid xenon as target material as well. The most stringent limit in the lowest mass range (below 1.6 GeV/c^2) is set by the CRESST collaboration, which detects phonons and light using scintillating calcium tungstate crystals [23]. In the intermediate range, the search is led by the CDMS collaboration, operating cryogenic germanium detectors aiming for simultaneous phonon and ionization detection [24].

1.2 The XENON dark matter experiments

Since 2006 the XENON detectors have been seeking WIMPs scattering off the nuclei of the element after which they are named. Settled in the underground Laboratori Nazionali del Gran Sasso (LNGS), the detector is shielded from cosmic radiation by 1.4 km of rock, corresponding to 3.4 km of water equivalent [25]. The first detector within a series, XENON10, featured a total mass of 15 kg and set the design and working principle for its predecessors [26]. The next upgrade, XENON100, was first deployed in 2009 counting a total mass of about 160 kg and led the dark matter search placing the most stringent limits of SI and SD WIMP-nucleon interactions at that moment [27]. In the course of writing, the XENON1T was recording science data utilizing a total xenon mass of 3.4 tons. Combining two science runs starting in November 2016, the achievement was very recently repeated. This thesis was written in the framework of XENON1T and its imminent upgrade, XENONnT, with an increased total mass of 8 tons. Therefore, the operation principle of these detectors is outlined in this section.

1.2.1 Detection principle

The dual-phase time projection chamber (TPC) is the innermost element of the XENON experiments and contains the liquid xenon (LXe) target as well as the gaseous xenon (GXe) phase on top. Figure 1.4 sketches its geometry and working principle. Two arrays of photomultiplier tubes (PMT) each located at the top and bottom surfaces of the chamber scan the xenon in the volume. When a particle scatters in the liquid xenon, it emits scintillation photons and ionization electrons. The scintillation light, referred to as prompt signal or S1, is immediately detected by the PMTs. Meanwhile, the ionization electrons are drifted upwards by means of the homogeneous electric field E_{drift}. Once they arrive at the liquid-gas interface, they are pushed through a grounded gate grid by means of the subsequent stronger extraction field $E_{\text{extraction}}$ and into the gas phase. There, the xenon atoms produce a second scintillation signal S2, by electroluminescence proportional to the number of ionization electrons [29]. The S1/S2 ratio is the basic tool for discriminating between collisions with the xenon nuclei (nuclear recoil) and with electron shell (electronic recoil). The former is the expected signature of a WIMP event as well as neutrons, while the latter is usually due to β or γ-radiation. Furthermore, the time lapse between the occurrence of the S1 and S2 signals can be converted into the vertical position (Z) of the vertex by multiplying it times the electron drift velocity. Additionally, the XY-position of the vertex is reconstructed from the S2 signal hit pattern in the top PMT array, leading to a full 3D position reconstruction of each event. This permits

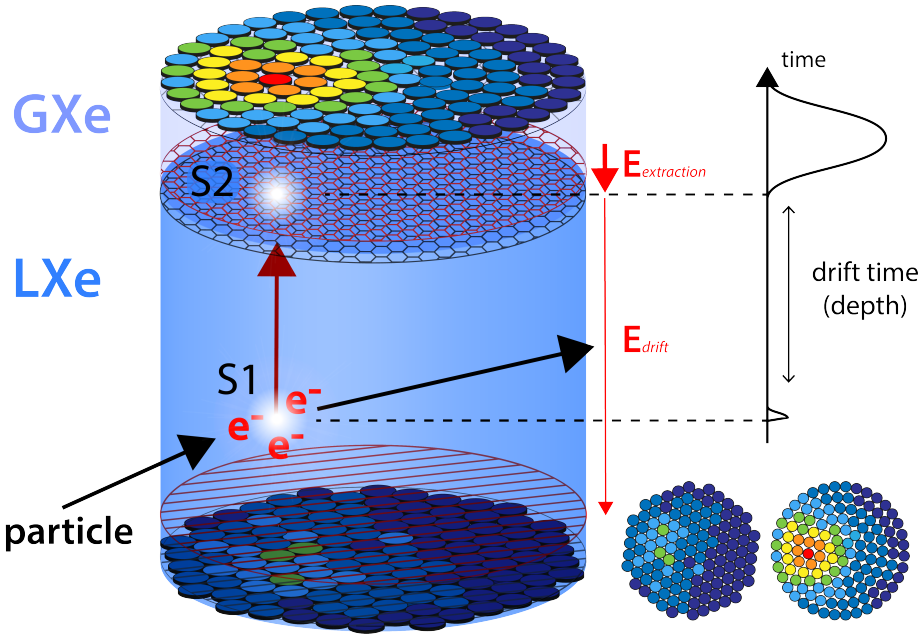

Figure 1.4: Working principle of the XENON detector. Figure extracted from [28].

the fiducialization of the operating volume, i.e. limiting the science data to a defined inner volume isolated from background events taking place at the edges of the chamber. This way the self-shielding properties of xenon are fully utilized to reduce the radiation coming from the surroundings. This radiation comes from radioactive decays in the detector materials.

Polytetrafluorethylen (PTFE) is used to house the PMTs in the TPC for several reasons: it efficiently reflects the scintillation light so that the photon collection is maximized [30], it serves as electrical insulator of the high voltage ($\sim$ 10 kV) drift field and it is reasonably radio-pure. However, exposure to air containing traces of radon or other contaminants can compromise this last feature. This work deals with strategies for mitigation of such contaminants of PTFE in chapters 3 and 4. In the following section we briefly review the different sources of background affecting both the nuclear recoil (NR) and the electronic recoil (ER) signals. In chapter 2 we focus our attention on the background induced by ^{222}Rn and the methods to mitigate it.

1.2.2 Background sources and reduction strategies

Figure 1.5 illustrates the simulated energy spectra of different sources of background in 1 ton fiducial volume (FV). The regions of interest (ROI) in the spectra are determined by the expected nuclear recoil (NR) of a WIMP. This is below 50 keV, which translates in about 12 keV for electronic recoil (ER) [31]. The dominating source in the NR spectrum comes from radiogenic neutrons. PTFE has a high neutron yield and is therefore one of the critical neutron producers [32]. The main path to suppress this source is the aforementioned fiducialization technique.

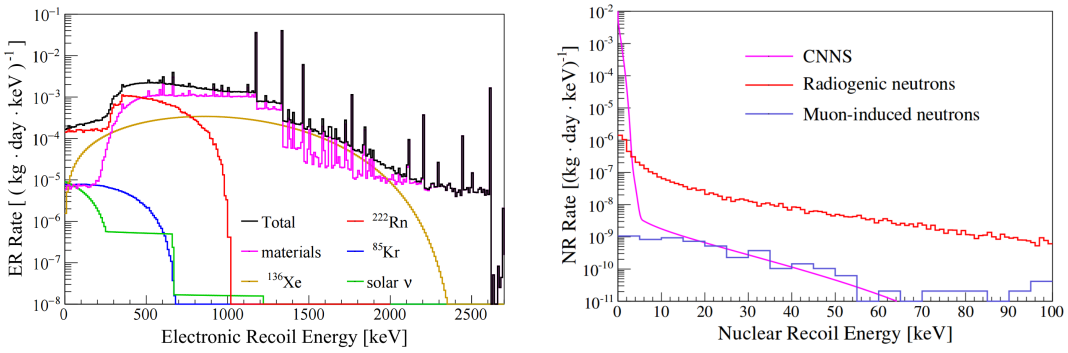

Figure 1.5: Simulated contributions from different sources to the energy spectra. Left: electronic recoil (ER) spectrum. The dominating source is ^{222}Rn (red) for the region of interest, i.e. for energies $\lesssim$ 250 keV . Right: nuclear recoil (NR) spectrum. Figure extracted from [31].

The background caused by muon-induced neutrons is effectively reduced by the active Cherenkov muon veto [33]. A water tank scanned by 84 PMTs is used to detect and veto cherenkov light signal produced by muons traveling across it. Furthermore, the water tank provides shielding against γ-rays from natural radioactivity occurring in the experimental hall. An additional neutron veto based on a gadolinium-loaded liquid scintillator is proposed for the upgrade of the detector with XENONnT [34].

Lastly, an unavoidable source of NR background is that produced by coherent neutrino-nucleus scattering (CNNS) from solar neutrinos, as modeled in [19].

On the other side, the ER includes two irreducible sources: solar neutrinos and two-neutrino double-beta decay ($2\nu\beta\beta$) of ^{136}Xe. We refer to [31] for further details on these sources. The contribution of ^{222}Rn clearly dominates ($\sim$85%) in the region $\lesssim$ 250 keV, as shown in figure 1.5. Its presence in the detector and the different strategies to mitigate it are discussed in section 2. The major contribution at higher energies is that induced by gamma emissions from the detector materials. This contribution is mitigated by fiducialization and thorough selection of the materials used [35]. Germanium spectroscopy [36] is utilized to quantify the activity of the materials coming from gamma emitters in the spectrum ROI.

The krypton concentration in commercial xenon ranges between 10 ppb and 1 ppm. The anthropogenic β-emitter ^{85}Kr appears in Europe with an isotopic abundance of $2 \cdot 10^{-11}$. An homogeneous flux of krypton is therefore introduced in the TPC mixed with the xenon. However, the vapor pressure of the former noble gas is 10.8 times larger than that of the latter. A cryogenic distillation column was developed to exploit this property [37]. It is sketched in figure 1.6. The xenon mixed with krypton is liquefied and injected in the 2.8 m column containing structured stainless-steel package material which provides a large surface. The xenon is liquefied by a condenser located at the top of the column and it flows to the bottom reservoir where a reboiler heats it. This way, a stream of xenon travels through the package where it condenses on its way up and evaporates on its way

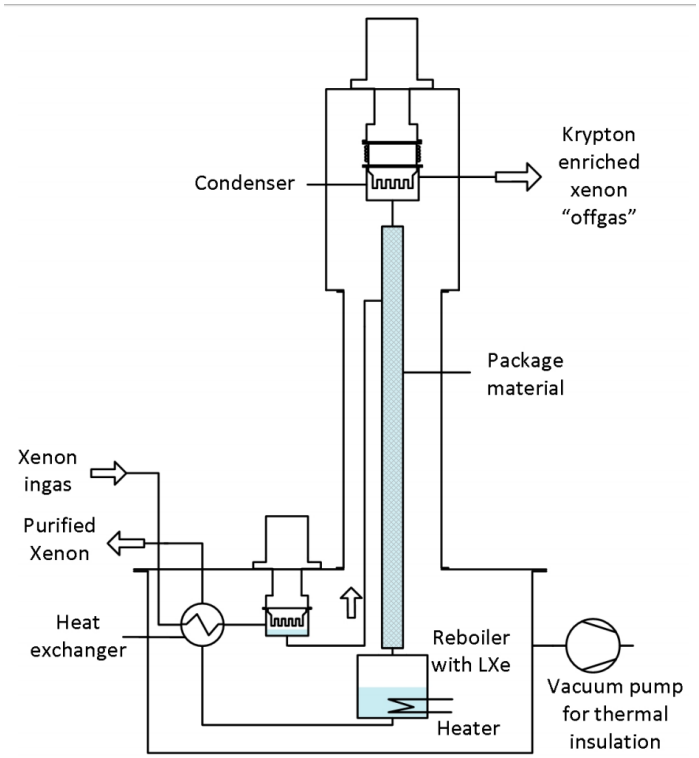

Figure 1.6: Structural scheme of the krypton distillation column. Figure courtesy of [37].

down. Krypton-enriched xenon accumulates at the top of the column and a small fraction of it is extracted, whereas purified xenon is collected at the reservoir and is circulated back to the detector. The achieved concentration of krypton was below 0.5 ppt, greatly suppressing its background contribution.

2 Radon Background in XENON1T

Several background mitigation strategies have been mentioned in section 1 concerning cosmic radiation and krypton. Nevertheless, the currently dominant contribution to the background is due to ^{222}Rn and it is the object of study in this section. Radon is the only naturally occurring noble gas with no stable isotopes. Its noble gas nature starkly limits its chemical reactivity and enhances its diffusion length through any material [38]. This results in an effect known as radon emanation: ^{222}Rn is produced via radioactive decay within some substrate and it leaves its original position through diffusion or through radioactive recoil. Due to its relatively long half-life of $\tau_{\mathrm{Rn222}} = 3.82$ days, it can cover large distances before undergoing further disintegration. Hence, it is able to reach critical parts of the detector.

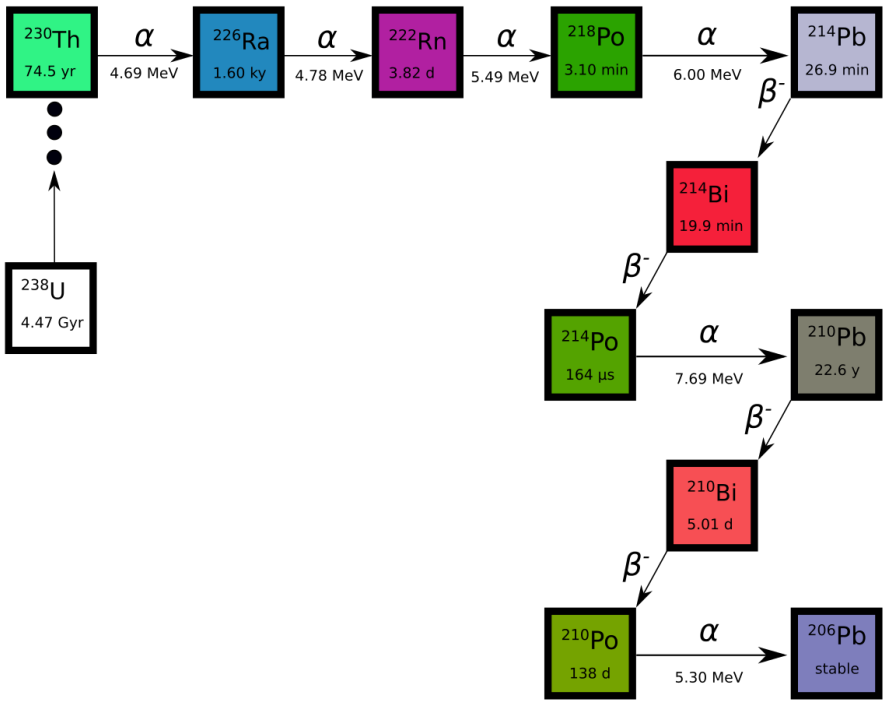

Figure 2.1: Excerpt of the ^{238}U decay chain featuring ^{222}Rn and its highly probable decay products (with branching ratio larger than 1%). Data from [39].

An extract of the ^{238}U decay chain containing ^{222}Rn is shown in figure 2.1. The decay series evidences possible sources of ^{222}Rn production: traces of ^{238}U and ^{226}Ra contained in many construction materials. Additionally, ^{220}Rn, generally referred to as "thoron", can also be emanated and introduced in the detector. It belongs to the decay chain of ^{232}Th, which is present in the construction materials too. Nevertheless, ^{220}Rn has a much shorter half-life of 56 s [39], so the probability that it is diffused into the detector is strongly suppressed [31]. Thoron contributes with

a concentration smaller than 0.1 μBq/kg, whereas ^{222}Rn with 10 μBq/kg. Therefore, in this section we will focus on ^{222}Rn, referred to as "radon" hereafter, as a source of intrinsic background in XENON. Thoron, in particular its isotope ^{212}Pb, will be the object of study of section 4.

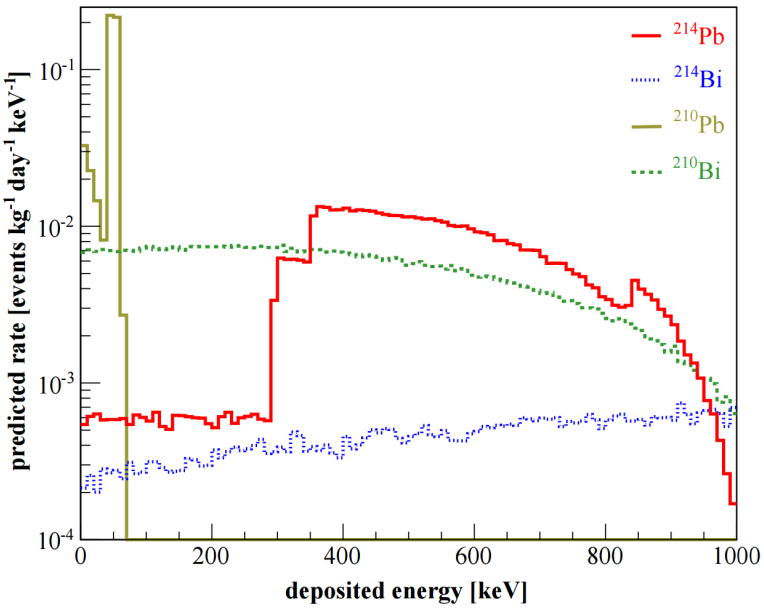

Figure 2.2: Simulated background rate contribution from β-decays in the ^{222}Rn chain. The dominant emission is that of ^{214}Pb (solid red) due to simultaneous γ-emissions. Courtesy of [40].

2.1 Background induced by radon daughters

The impact of the decay products of ^{222}Rn on the background of XENON will be analyzed in this section. Figure 2.1 summarizes the α and β-emission from radon and its daughters. The case of α emissions is likewise negligible as their energy depositions are far too energetic compared to the region of interest (ROI) for WIMP searches ($\sim$ 100 keV).

On the contrary, the continuous β-spectra spans over the keV scale, raising the background signal in the ROI. As figure 2.1 sketches, the chain of ^{222}Rn contains four β-emitters: ^{214}Pb, ^{214}Bi, ^{210}Pb and ^{210}Bi. Their energy spectra are shown in figure 2.2. These decays were simulated in a 1 ton liquid xenon target using Geant4 software and assuming an initial activity of 60 μBq/kg for each isotope [40]. The most critical contribution is the one induced by ^{214}Pb. About 90% of these events can be discriminated as they occur with a simultaneous γ-emission which allows for its identification and rejection. The contribution from gammas is reflected in the shape of the ^{214}Pb spectrum as a sudden increase of about an order of magnitude for energies $\gtrsim$ 300 keV. The spectrum from ^{214}Bi is subdominant in the scale $<$ 1 MeV and it accompanied by a immediate α emission of ^{214}Po ($\tau_{\mathrm{Po214}} = 164$ μs). This coincidence permits an effective event rejection of more than 50% [40]. For energies $\lesssim$ 400 keV, ^{210}Pb and ^{210}Bi dominates as visible in figure 2.2. However, the

simulation assumes the same initial activities for all the isotopes, i.e. secular equilibrium. This condition does not apply for the detector conditions in that the intrinsic ^{222}Rn produced by decay of ^{226}Ra within the construction materials is not in equilibrium with ^{210}Pb (thus neither with ^{210}Bi). This is due to the long half-life of ^{210}Pb, 22.3 years, much longer than the prospect operating time of XENON1T. For this reason the contributions of ^{210}Pb and ^{210}Bi are neglected in the intrinsic background computation.

A different situation is that of the so-called "surface background". This refers to radiation emitted from the TPC walls by isotopes sitting on the PTFE. These isotopes originate from plate-out of radon daughters on the PTFE during the time previous to the detector assembling. The electronegative fluorine atoms of PTFE makes it prone to carry static negative charge [41]. That, together with the fact that 88% of the radon decay products are positively charged [42] results in an enhanced plate-out rate of radon daughters on PTFE compared to other materials. ^{210}Pb and the subsequent progeny contribute to the detector background in this manner. This is the dominating process by which ^{210}Pb enters the detector.

One concern of plate-out radon daughters is neutron production. The alphas emitted by ^{210}Po feeds (α,n) reactions of the fluorine in the PTFE, due to its high neutron yield [32]. Additionally, ^{210}Pb and ^{210}Bi emit bare betas which can be rejected through fiducialization. However, the reconstruction algorithms suffer from inhomogeneities of the electric field. As a consequence surface events can be misreconstructed inside the fiducial volume. Moreover, the S2 signals from suface decays feature lower intensity due to drift electrons being lost by colliding with the TPC walls. Therefore, a lower S2/S1 ratio is measured, compatible with a false nuclear recoil signature. Under this premise, removal techniques of long-lived radon daughters are investigated in section 3.

2.2 Mitigation techniques for radon-induced intrinsic background

In this section we outline different strategies to reduce the intrinsic background of XENON originated by radon progenies. The reader interested in further details of the techniques presented here is referred to [43],[44] and [45]

2.2.1 Material selection

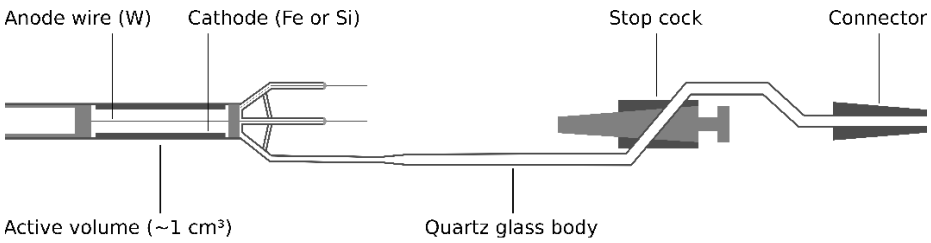

Figure 2.3: Miniaturized proportional counter. Figure from [46].

The basic ingredient for a reduced intrinsic background is a careful selection of the materials used in the construction of the detector. Critical components are those in direct contact with the xenon, for instance the PMTs, the PTFE panels in the TPC and the cryostat which houses it. During an extensive screening campaign, previous to the assembly of the detector, all the materials undergo a measurement of its radon emanation rate. The samples are stored in a vessel for a few days and the emanated radon is collected and flushed through a purification gas line. This features activated charcoal traps and a hot getter to separate the radon from other impurities. Afterwards, the radon is pushed using mercury into a miniaturized proportional counter where its activity is measured [44]. These detectors were originally developed for the GALLEX solar neutrino experiment and are handcrafted at the Max Planck Institute für Kernphysik (MPIK). One of such detectors is shown in figure 2.3. With this method, a sensitivity on radon activity in the scale of $\sim 20\mu$Bq is achieved [44].

2.2.2 Radon distillation column

A radon removal system was tested achieving a reduction of ^{222}Rn by a factor $\gtrsim 27$ (95% CL) [47]. Its working principle is based on the higher vapor pressure of xenon with respect to that of radon and its structure is the same as the krypton distillation column shown in figure 1.6. The main difference with respect to the latter is that in this case radon-enriched xenon accumulates in liquid in the reservoir at the bottom of the column where it remains until the radon decays away. This implies that the xenon can be reused instead of being extracted and discarded. Moreover, krypton is distilled only once during the commissioning stage of the detector whereas radon, being constantly emanated from the materials, needs to be removed continuously by this method during the operation of the detector. This setup is scheduled to be incorporated to the upgrade XENONnT.

2.2.3 Coating

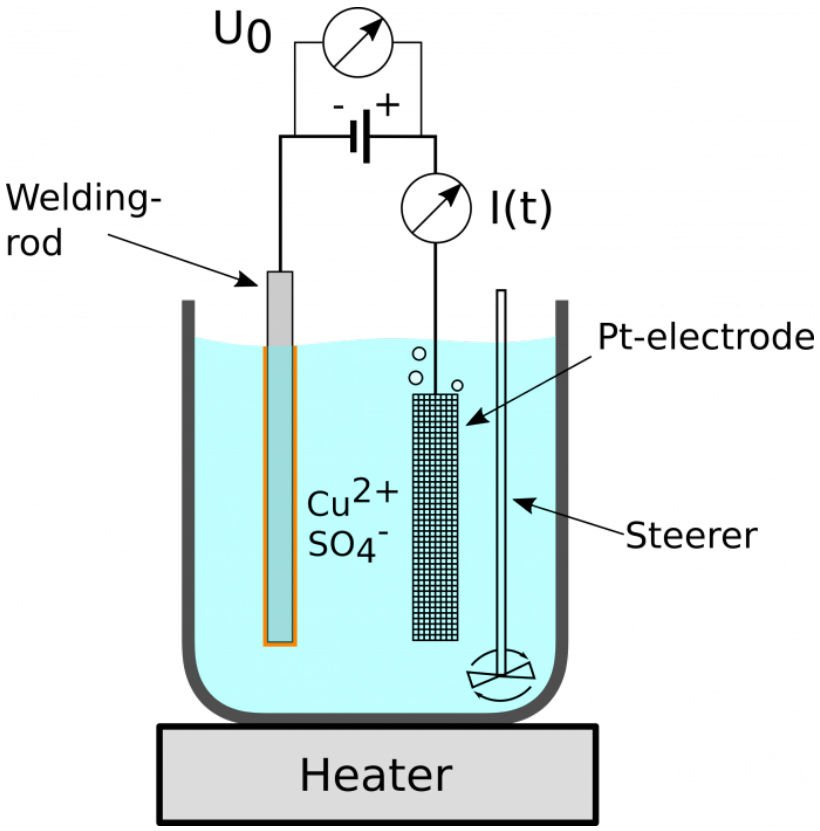

Figure 2.4: Sketch of the setup for electrodeposition. Figure from [45].

Another radon-mitigation technique consists on coating the surfaces of critical detector parts with an ultra-pure material. This way a radon-free layer covers the outermost surface of the material jeopardizing the emanation of radon within deeper layers. Several coating methods were investigated, so as their resulting reduction capabilities and layer properties [45]. Figure 2.4 displays the setup used for one of these methods: electrodeposition. A solution containing $CuSO_4$ is heated up to a temperature of $\sim 50°C$, steered in a beaker. A potential difference is applied between the workpiece (a welding-rod in the figure) and a platinum electrode driving the copper ions in the solution to the surface of the sample. The deposited mass can be inferred from the current measured between the electrodes, since it gives information on the total charge and thus on the number of copper atoms deposited on the sample. A reduction factor of $\sim$8 of ^{222}Rn was reached this way.

3 Removal of radon daughters from PTFE surfaces

3.1 Motivation: PTFE in XENONnT

At the end of section 1.2.1 we saw the applications of PTFE in the TPC of XENON as electric insulator and light reflector. Furthermore, in section 2.1 we detailed how ^{222}Rn in air plates-out its daughters onto the PTFE surface and how the decay of long-lived daughters contributes to the so-called surface background of the detector. In this light, a study on the removal of long-lived radon daughters from PTFE surfaces was carried out and is outlined in this section. This chapter is structured as follows: the detectors used for the study, the alpha-spectrometers, is described in section 3.2, so as the main features of the measuring procedure. In section 3.3 we detail the cleaning procedure which were tested and their efficiency at removing ^{210}Po from PTFE surfaces. In section 3.4 an analysis of the efficiency of those procedures at removing ^{210}Pb is explained. Finally, in section 3.5 we investigate the shape of the obtained ^{210}Po peaks in the spectra.

3.2 Alpha-spectrometer characterization

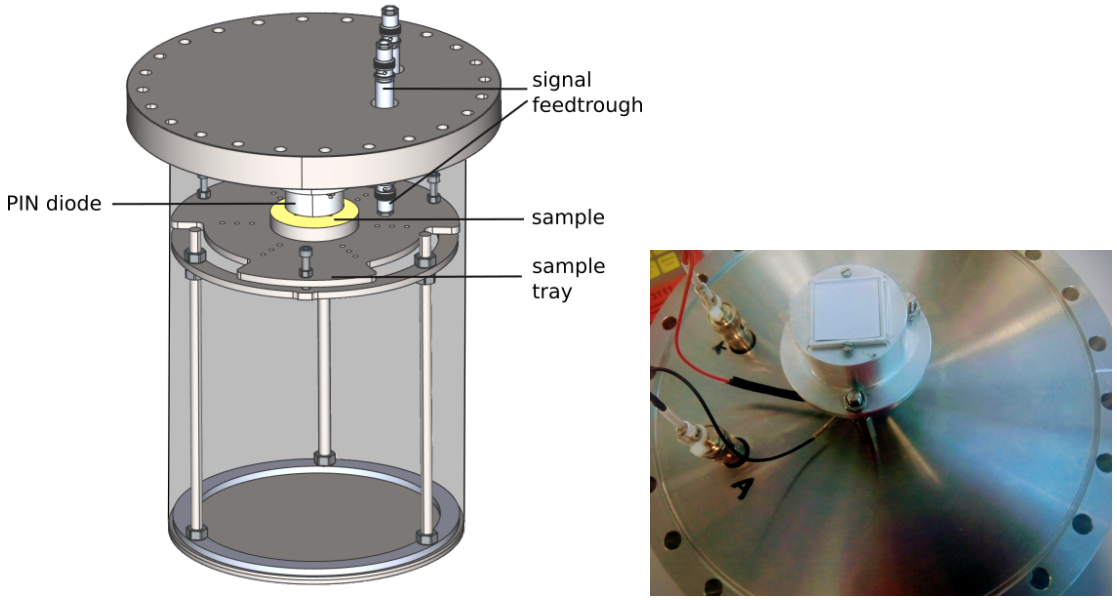

Figure 3.1: Left: Structural scheme of the alpha spectrometer. Right: Front view of the top flange, the diode's detection surface and feed-through connection.

In this section we outline a brief characterization of the detectors used to measure the abundance of radon daughters in the studied samples. Two detectors were employed for this work. Each one featured different sizes but the same cylindrical geometry and working principle. Figure 3.1 (left)

shows the schematic structure of the first, larger detector, which will be referred to as surface alpha-detector. The main detection component is also displayed in figure 3.1 (right): a silicon PIN diode of approximately 13 mm of size (1.7 cm^2 of total surface). Larger diodes for higher sensitivity are intended to be purchased in the future. In this detector, the sample is set, coaxial and parallel to the diode, on a tray whose height can be adjusted at wish. The vessel containing the sample and the diode has a volume of 9.2 L, and it is continuously evacuated during the measurements, so that the alphas can reach the detector without colliding with air molecules. This spectrometer was designed and manufactured at the Max Planck Institute für Kernphysik (MPIK), in Heidelberg.

The second, smaller detector was also built at MPIK but it was originally designed as an electrostatic collection radon monitor [48]. During the construction of the surface alpha-detector, this one was adapted to act as a second alpha spectrometer. It is referred in this work as RaMon. For this study we attached a plastic sample holder underneath the PIN diode in order to keep the distance between them minimal and fixed. The vessel fits a volume of about 1 L. Both PIN diodes are identical in shape and manufacturer.

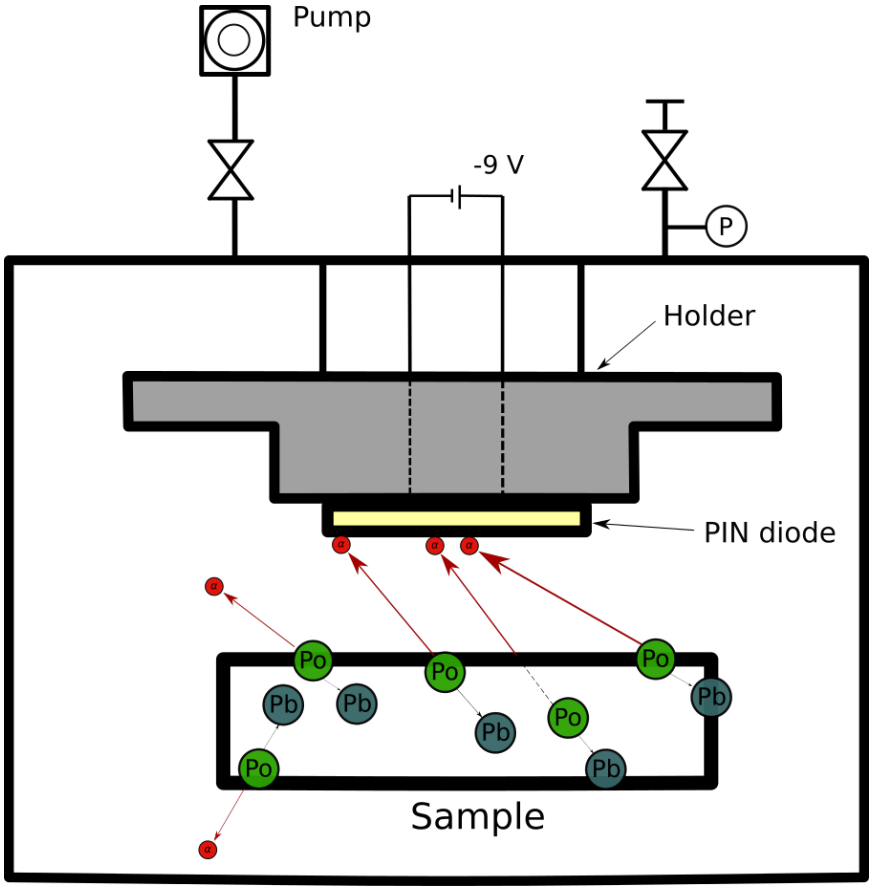

Figure 3.2: Sketch of the collection principle of the alpha spectrometer. α-particles (in red) are emitted by polonium (green) disintegration and get detected when reaching the PIN diode.

Figure 3.2 depicts the basic operating principle, common to both detectors. The radon daughters (in the image polonium) sitting on the surface of the sample or within its bulk, decay to the next isotope in the chain (in this case lead), which gets a recoil energy. In this process, an alpha is emitted (in red) which can reach the PIN diode. Alphas emitted from the very surface deposit its full energy in the detector whereas those traveling through the bulk lose a fraction of it by colliding with other atoms. Electron-hole pairs are produced in the substrate of the PIN diode proportionally to the energy deposition of the alphas. The 9 V reverse bias allows a current flow of the pairs. This current is then amplified and transformed into a digital signal by mapping each current value (thus each deposited energy) to a channel in the spectrum.

3.2.1 Detector calibration

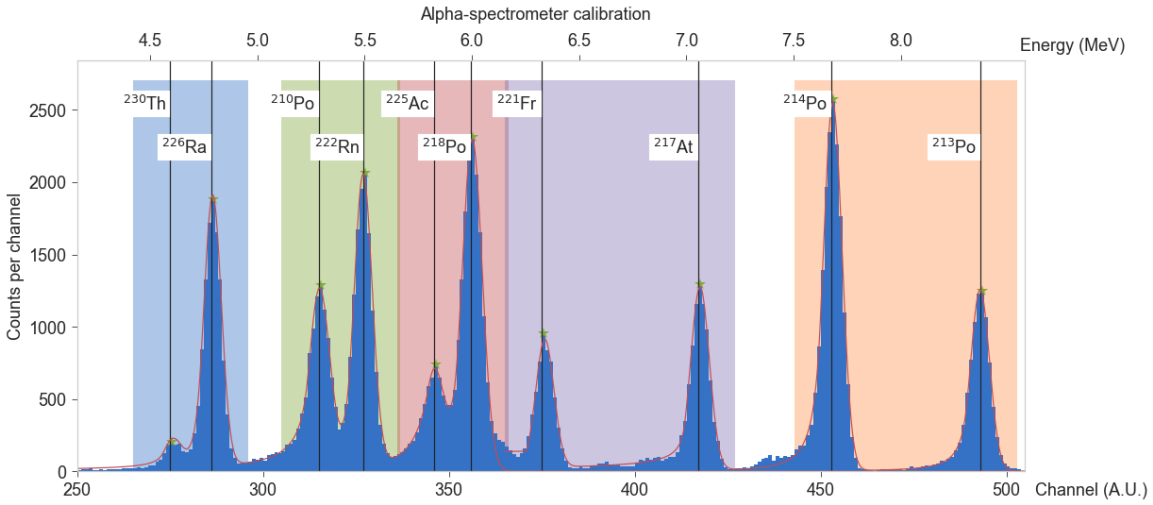

Figure 3.3: Spectrum used to calibrate the detector response featuring multiple peaks from α-emissions. The filled regions correspond to five separate intervals of the spectrum, each of which was fitted to the sum of two crystalball functions (see text).

An example of spectrum recorded with the setup appears in figure 3.3. This spectrum corresponds to a stainless steel sample contaminated with short-lived isotopes in the decay chains of ^{238}U and ^{237}Np. They were known from a previous screening measurement of the sample [45]. The spectrum was used to calibrate the energy scale corresponding to the different channels: First, each peak was fitted to a crystalball function, which consists of a gaussian part on the r.h.s. and a power function of order n on the lower tail to describe the loss of energy of the alphas [49].

$$f(E;\mu,\alpha,n,\sigma) = N \cdot \begin{cases} A \cdot \left(B - \frac{E-\mu}{\sigma}\right)^{-n}, & \text{for } \frac{E-\mu}{\sigma} \leq -\alpha \\ \exp\left(-\frac{(E-\mu)^2}{2\sigma^2}\right), & \text{for } \frac{E-\mu}{\sigma} > -\alpha \end{cases}, \tag{3.1}$$

where

$$A = \left(\frac{n}{|\alpha|}\right)^n \exp\left(-\frac{|\alpha|^2}{2}\right),$$
$$B = \frac{n}{|\alpha|} - |\alpha|,$$

and N is a scaling parameter. The fit parameter μ, the expected value in the gaussian part, corresponds to the maximum deposited energy of the alphas[1].

Once the central value of all the peaks is known, their corresponding deposited energy must be inferred. The position of the ^{210}Po decay was taken as reference. This isotope is known to be implanted on the diode during previous exposure to ^{222}Rn. Consequently, long-lived radon daughters (^{210}Pb and ^{210}Po) have been plated-out onto the diode and the detector's walls, causing a constant background. This is the main contribution to the background activity of the detector as we will see in section 3.3.2.

The diode's response was known to be linear in the energy range investigated in this work [45]. This was checked by plotting the literature value of the alpha decays, Q_α, as a function of the mean channel values, as figure 3.4 demonstrates. A straight line was fitted to these points and the resulting function was used to calibrate the energy scale.

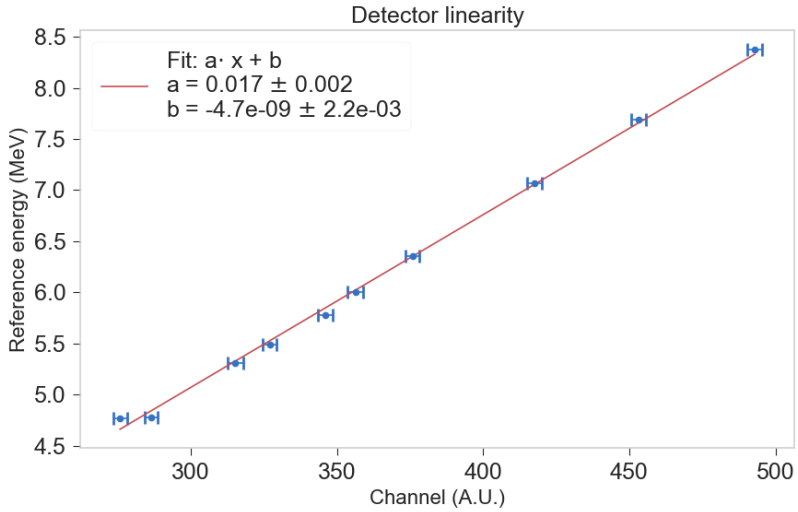

Figure 3.4: Linearity response of the diode: On abscissa the mean values of the peaks are arranged, on ordinate the Q_α-values of the alpha decays of the found isotopes.

The deviation of the first point might be caused by a misidentification of the isotope or by the limited resolution. Since the main region of interest in the spectrum is above this energy value (4.8 MeV), the fit was kept. The energy resolution was estimated as the FWHM of the peaks and was found to be around 0.1 MeV.

[1] Assuming that they are emitted directly from the sample's surface.

3.2.2 Detection efficiency

The counting rate measured by the spectrometer was corrected using for the geometric detection efficiency, which was estimated through a Monte Carlo simulation.

The simulation is illustrated in figure 3.6. First $N \approx 30000$ particles are generated uniformly and isotropically over the disc centered on the coordinate origin. Then, for each particle, the momentum-direction vector is randomly generated and the particle is translated to a height d, leading to the coordinates:

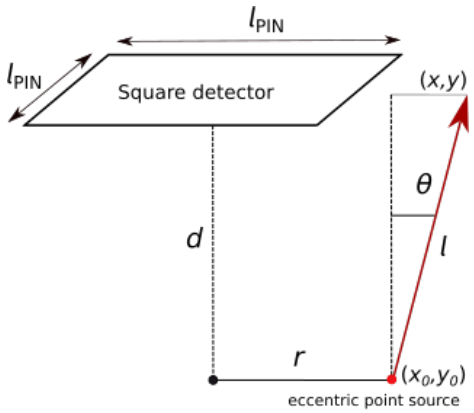

Figure 3.5: Sketch for geometry efficiency calculation.

$$\begin{aligned} x &= x_0 + l \sin\theta \cos\phi \\ y &= y_0 + l \sin\theta \sin\phi \\ z &= z_0 + d, \end{aligned} \tag{3.2}$$

in which $l = \frac{d}{\cos\theta}$ (see the geometry in figure 3.5). The particle is detected if

$$|x| \leq l_{\text{PIN}} \quad \wedge \quad |y| \leq l_{\text{PIN}},$$

where l_{PIN} is the side length of the diode. Then, the detection efficiency is simply

$$\varepsilon = \frac{1}{2} \frac{N_{\text{det}}}{N_{\text{tot}}}. \tag{3.3}$$

The factor 1/2 takes into account the particles which can be emitted downwards, which were not initially generated for faster computation. The simulation is illustrated in figure 3.6. The results for several relative sizes and distances are depicted in figure 3.7.

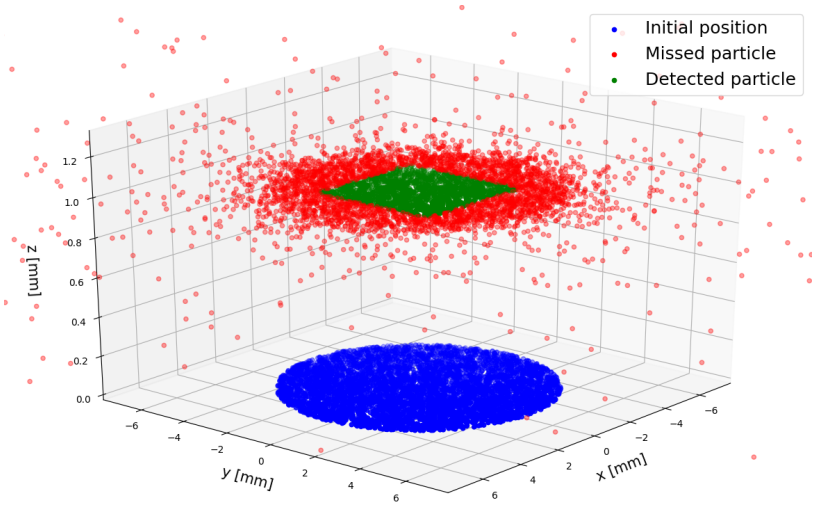

Figure 3.6: Solid angle simulation for the experimental conditions: square detector and circular source .

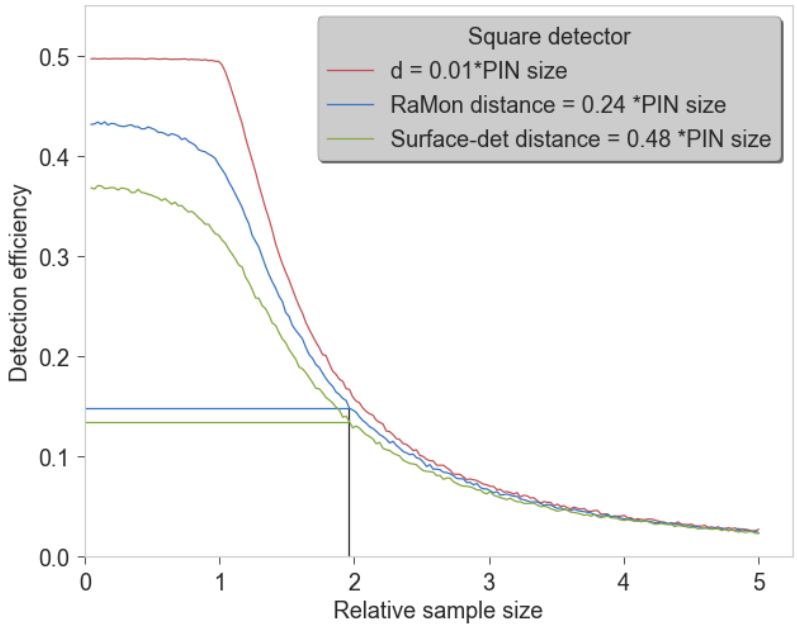

Figure 3.7: Simulation result for the setup conditions.

The samples' diameter and the PIN diode's side were identical for all measurements. The distance between them was also kept constant throughout all the measurements but differed for each detector. Table 1 summarizes these experimental conditions as well as the efficiencies calculated using the simulation. To obtain these results, the simulation was run 1000 times, with fixed conditions, and the average and standard deviations computed.

$$r_{\text{disc}} = (25.00 \pm 0.15)\ \text{mm}$$
$$l_{\text{PIN}} = (12.74 \pm 0.15)\ \text{mm}$$

	distance [mm]	ε_{sim}
Surface detector	6.2 ± 0.9	0.136 ± 0.002
RaMon	3.1 ± 0.6	0.151 ± 0.002

Table 1: Experimental conditions and geometric efficiencies.

Analytic expressions for a circular detector and homogeneous circular source can be found in the literature as well [50][51][52].

3.2.3 Handling of the systematic uncertainty

Considering the long half-lives of the investigated radon daughters, ^{210}Pb and ^{210}Po, the activity of the samples is expected to remain constant between two measurements in the same cleaning stage. Nevertheless, the measurements presented noticeable systematic fluctuations, probably linked to an inhomogeneous loading of the sample.

The systematic uncertainty was estimated, separately for each detector, by computing the relative deviations of each measurement from the average corresponding to each cleaning stage. Then, these deviations were arranged in a histogram, as depicted in figure 3.8. The systematic uncertainty was determined as the sigma of the gaussian fitted to such distribution. This uncertainty is then added to the usual poissonian statistical uncertainty for each measurement.

In order to account for the effects of ^{210}Po evaporation and ^{210}Pb removal, which are detailed later in this chapter, we used only sets of measurements within short time lapses (not longer than two weeks) for this systematic error estimation.

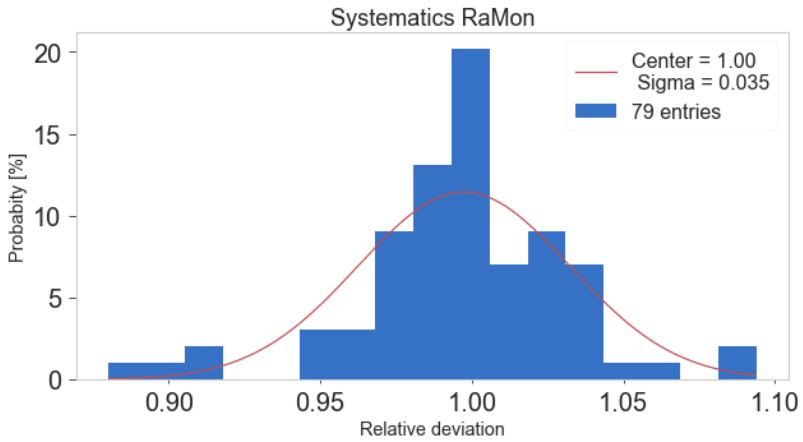

Figure 3.8: Systematic error distribution of the samples' measured activities during short time intervals.

3.3 Removal of ^{210}Po

As outlined in section 2.1, α-emissions from ^{210}Po sitting on the PTFE walls of the TPC can trigger (α,n) reactions which contribute to the nuclear recoil background in XENON. Hence, a study on the removal of this isotope from PTFE by means of surface treatment procedures was carried out and is discussed in this section.

3.3.1 Sample loading

In order to investigate the effect of different cleaning procedures, several PTFE samples artificially contaminated (loaded) with ^{222}Rn daughters were employed. The samples where flat discs of 50 mm diameter and 0.5 mm thick (see figure 3.9). To load these samples, they were inserted in a setup sketched in figure 3.10. ^{222}Rn emanates from uranium powder and mixes with the air contained in the vessel. The radon-enriched air is then brought, by means of a recirculation pump, to the sample vessel, where radon plates-out its daughters on the samples. The loading took place during several years previous to the measurements and was stopped about two years before them. Therefore, the ^{210}Pb implanted and the ^{210}Po measured can be assumed to be in equilibrium.

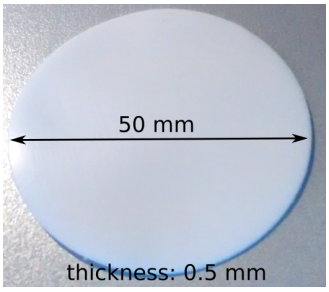

Figure 3.9: PTFE samples used for these studies.

One of the sides of the sample discs was directly facing the current of radon-enriched air. This led to a higher concentration of polonium on this side compared to of the opposite side.

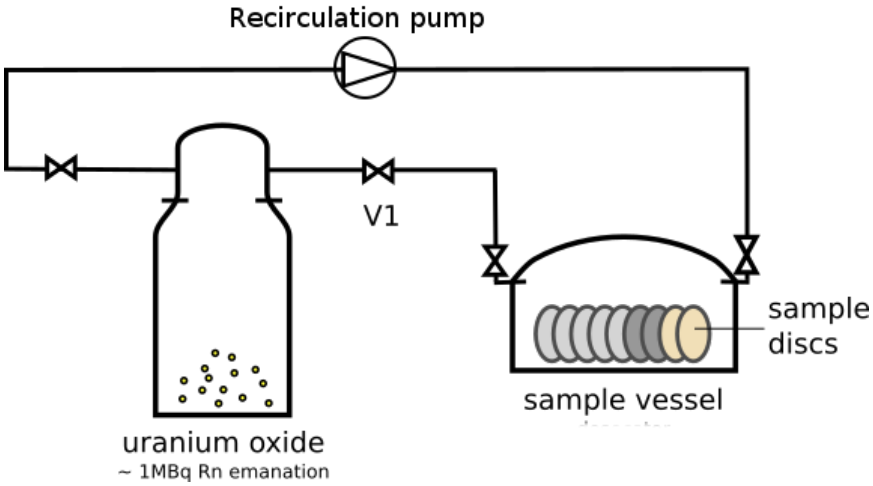

Figure 3.10: Setup for ^{222}Rn loading. The uranium source enriches air with radon which is then recirculated to the vessel where the samples sit.

Given the long half-life of ^{210}Po, $\tau_{1/2} = 138.4$ days, we expect the activity of the samples to stay

on a constant level during each measurement, which typically lasts around one day. Figure 3.11 depicts a typical spectrum of the ^{210}Po-loaded samples and the stability of the events within the energy interval corresponding to this peak. ^{210}Po is the only peak found in the full spectrum because it is the only long-lived alpha-emitting isotope (^{210}Pb is also present but emits betas) remaining in the sample.

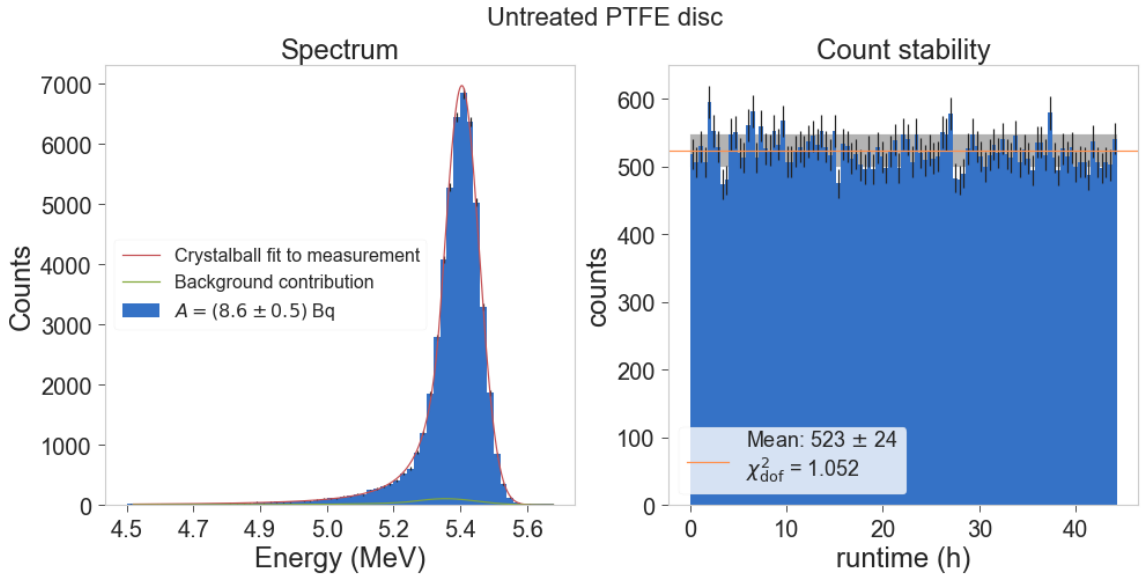

Figure 3.11: (Left) Alpha-spectrum of an untreated PTFE sample and fit to crystalball function. (Right). Time evolution of all the acquired ^{210}Po events.

3.3.2 Detector background

A contribution to the polonium activity registered in the detector comes from background events. As already noted, some polonium was implanted into the diode, its holding frame or into the detector walls during previous experiments where ^{222}Rn was present. This contribution was regularly monitored and must be subtracted when computing the activity of the sample. The background count rate of the two spectrometers are exposed in figures 3.12 and 3.13.

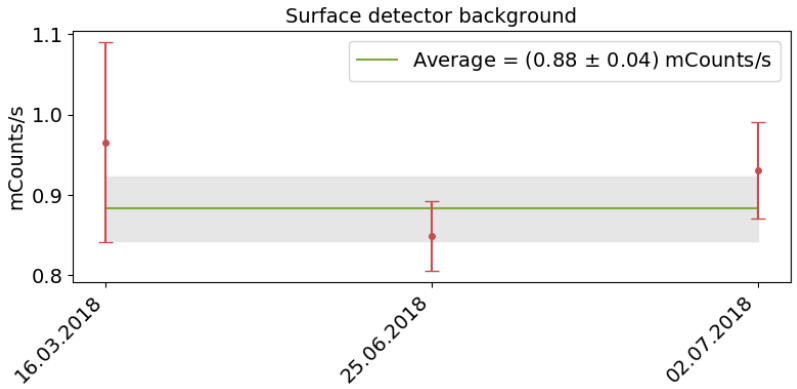

Figure 3.12: Background contribution to the ^{210}Po rate in the surface alpha-detector acquired during the measurement phase.

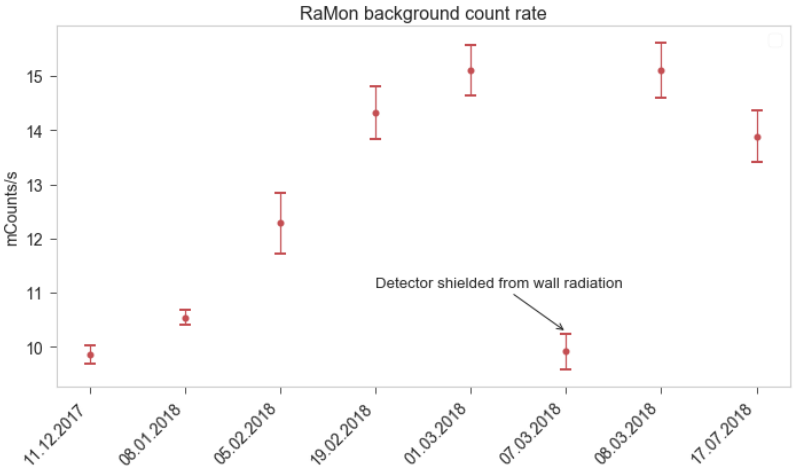

Figure 3.13: ^{210}Po background in RaMon. During the measurement carried out on the 7$^{\text{th}}$ of March, the diode was covered in order to isolate it from radiation coming from the detector walls.

On average, the background in the smaller detector (RaMon) is more than an order of magnitude larger. This reflects its longer previous utilization for highly emanating samples. The in-growth of the background rate is due to polonium being desorpted from the sample surface and migrating to the detector surfaces. This effect is further investigated in the following section. The background to sample signal ratio ranged from a 3% to 11%.

During the actual measurement of the PTFE samples, the detector was mainly shielded from the detector wall radiation by the sample holder, as the case indicated in figure 3.13 (data point 7th of March). Hence, this value was subtracted for the computation of the cleaning procedures reduction factor.

The background in the surface alpha-detector remained stable during the measurements, as shown in figure 3.12. This different behavior with respect to RaMon is due to the fact that the surface

alpha-detector was newly exposed to untreated sample discs. The effect of ^{210}Po-evaporation, in turn, occured only at measurements of uncleaned samples (see section 3.3.3).

3.3.3 Polonium evaporation

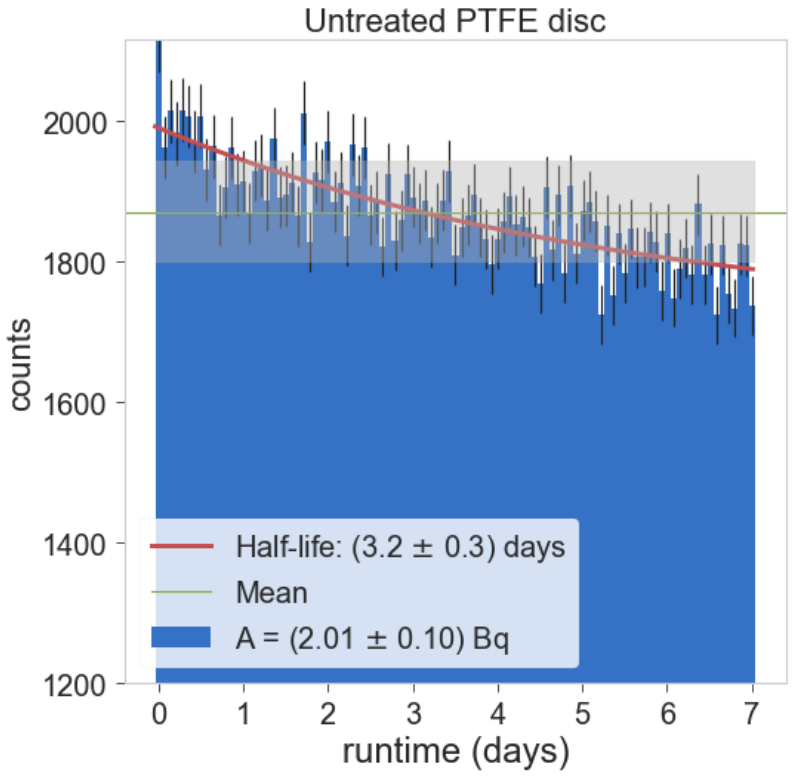

Figure 3.14: ^{210}Po evaporation during a measurement run two weeks long. Activity and mean value included for reference.

Several measurements of untreated samples showed a significant decrease of its polonium activity. An instance of such measurements is shown in figure 3.14. This decrease is much faster than the radioactive decay of ^{210}Po ($\tau_{1/2}$ = 139 days), so it cannot be linked to this cause. Moreover, the trend was clearly correlated with the time the sample had spent in vacuum, as depicted in figure 3.15. This time coincides with the detector's operating time, therefore it is referred as 'runtime'. Throughout all the measurements, the detector vessel was evacuated, exposing the disc to pressures of the range 10^{-2} mbar. Polonium may have been desorpted from the surface into the detector. Polonium evaporation has already been researched [53], [54]. Once the measurement was finished, the detector was filled with air in order to extract the sample.

For the first disc measured, a time lapse of several weeks passed during which the sample was stored at room pressure. Figure 3.15 shows the evolution of the untreated disc's activity during runtime (left), i.e. the time spent in vacuum, and during the actual time (right), including the

periods at which was exposed to air.

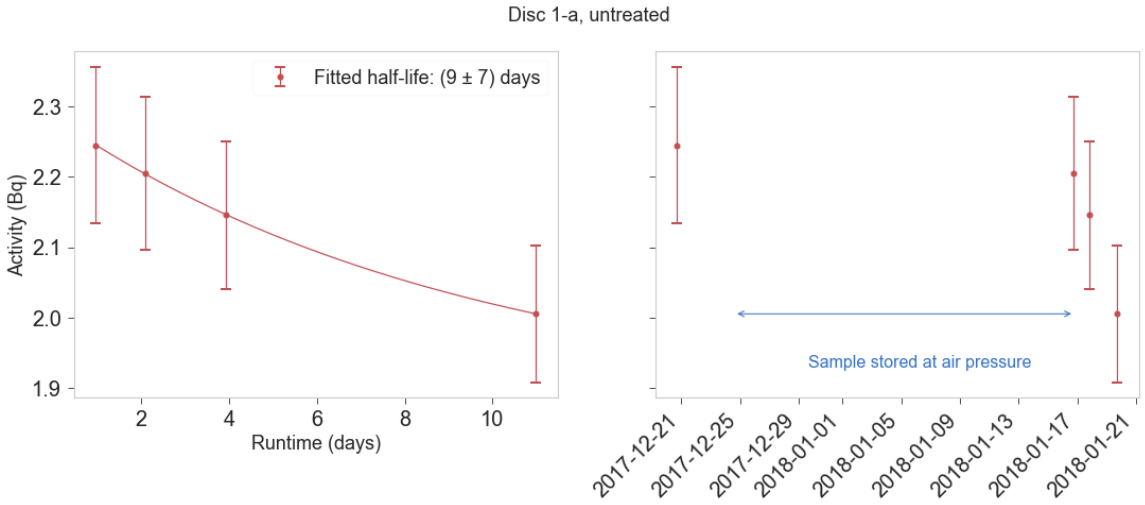

Figure 3.15: ^{210}Po evaporation. Showing as x-axis the total runtime of the measurements (a) and the 'timestamp' or actual time (b).

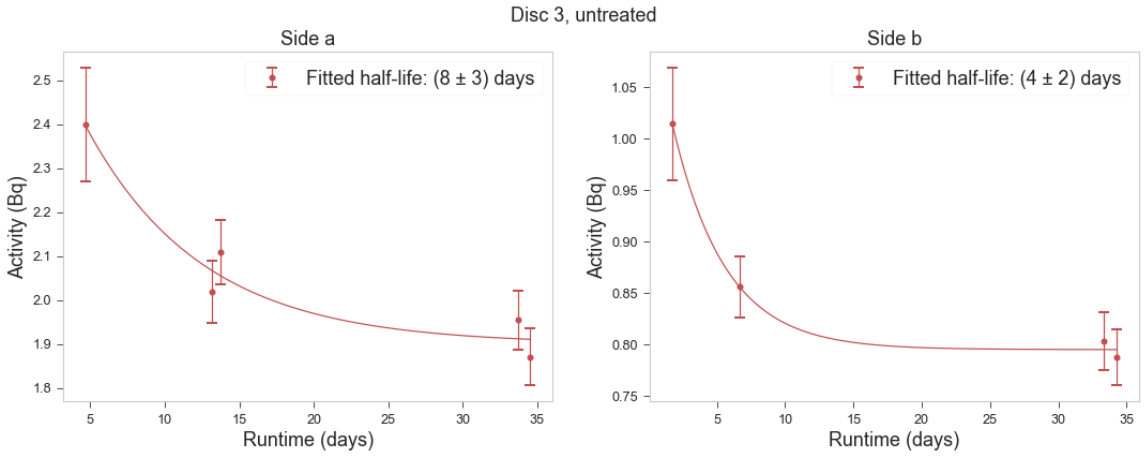

Figure 3.16: ^{210}Po evaporation on a different sample disc labeled '3'.

After applying the cleaning procedures the polonium did not noticeably evaporate anymore, thus its contribution to the background radiation decreased. This was the case of the last measurement in figure 3.13. This background measurement was carried out once the the sample's activity had reached a stable value, meaning that no desorption occurred anymore. Another case of polonium evaporation taking place in a different sample is shown in picture 3.16.

3.3.4 Tested cleaning procedures

Once a good set of measurements of the sample's activity prior to any treatment has been collected, we start applying different surface cleaning procedures. These are outlined below:

1. **Ethanol wipe:** Wipe with a cloth soaked in ethanol.
2. **Ethanol dip:** Bath in ethanol for 15-20 min.
3. **Weak nitric acid procedure:**
   (a) Immersion of the sample in 5% (by mass) HNO_3 dissolved in ultra pure water (UPW).
   (b) Sonication for 15 minutes. Then the sample is left in the bath for 2 hours.
   (c) Rinsing with de-ionized water.
   (d) Drying by blowing nitrogen.
4. **Strong nitric acid procedure:** Variation of the weak nitric acid procedure, using a HNO_3 solution of 6 mol/L (32%).
5. **Hot nitric acid procedure:** Variation of the strong nitric acid procedure: heating the solution to a temperature of 60 °C.
6. **Recirculated nitric acid procedure:**
   (a) Immersion in 6 mol/L HNO_3 solution and sonication for 15 minutes.
   (b) Immerse the disc in another glass with a fresh HNO_3 solution for 90 s. Reiterate this step a total of three times, every time with a fresh HNO_3 solution.
   (c) Rinsing with de-ionized water.
   (d) Drying by nitrogen blowing.

The weak nitric acid procedure on which all the variations are based is the standard procedure used in the XENON1T cleaning campaign for PTFE pieces and it preserves the material's UV reflectivity [30]. Furthermore, the "recirculated nitric acid procedure", is based on [55] and is intended to avoid redeposition of polonium solved in the acid back onto the PTFE surface during a long bath.

3.3.5 Observed ^{210}Po reduction

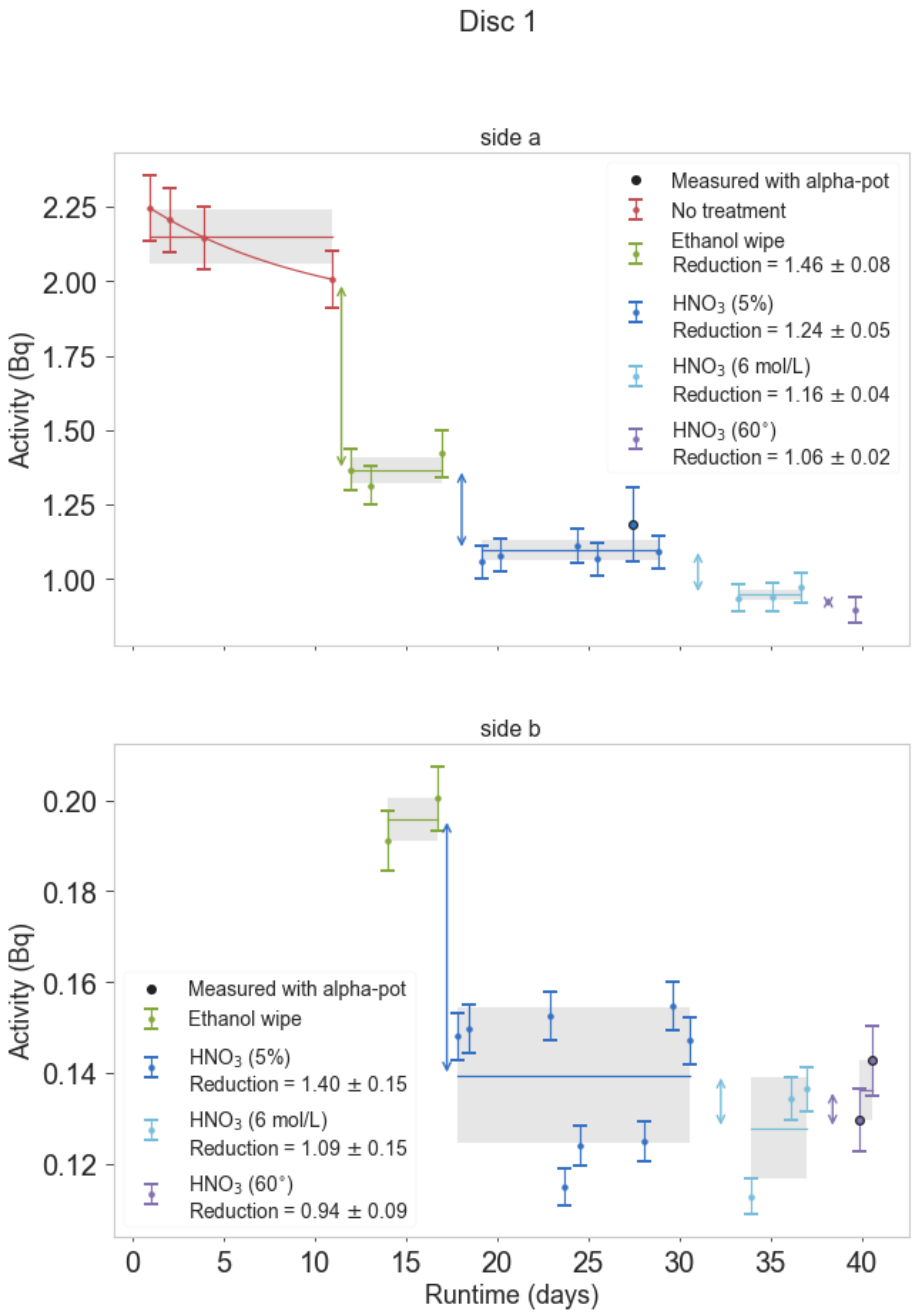

Figure 3.17: ^{210}Po activity of the samples before and after successive cleaning procedures. On the abscissa the accumulated runtime of each measurement is exhibited, i.e. the time that the sample spent in vacuum.

Figure 3.17 illustrates the calculation of the reduction factor observed after applying our cleaning procedures. The points in the plot represent a measurement of one of the four PTFE sample discs

used for this study. The disc was regularly flipped to measure the other side's activity too, which is treated as an independent sample. By convention, the more active side was referred to as 'a'.

The average activity and standard deviation of each cleaning phase are shown in figure 3.17 as a horizontal line and a shaded region around it respectively. From this quantities we compute the reduction factor as the ratio between the activity before and after the treatment:

$$R_{\mathrm{F}} = A_{\mathrm{pre}}/A_{\mathrm{post}}. \tag{3.4}$$

This calculation applies to all the reduction factors listed in this section except for the first treatment applied to each sample. In those cases, the following correction was taken into account: instead of taking the average activity of the sample before the treatment, since a clear exponential decrease trend appeared, the value of the activity at the time of applying the procedure was inferred from the fit. This fit is displayed in the figure too and hints to polonium evaporation, as argued in section 3.3.5. The error associated to the reduction factor, however, was computed from the weighted standard deviations.

Most of the measurements shown in this section were carried out using RaMon. For the measurements recorded by the surface alpha-detector an additional black marker is indicated in the graphs.

Disc 1 The effect of cleaning observed for sample disc 1 is depicted in figure 3.17 (both sides). First, the y-axis shows that radon plated-out more intensely on side 'a' by a factor 7.3 ± 0.3 with respect to side 'b'. Second, the more treatments we applied on the sample, the less effective they were, even though, for example, the third procedure was identical to the second but using a nitric acid solution concentration 5 times higher. This acid is known to be a good solvent for lead [56]. Lastly, the result from the hot HNO_3 procedure shows that heating the solution did not improve much the removal efficiency either.

An explanation for the decrease of the reduction factor would be the following: Most emitters sit on the surface of the disc or within the outermost layers of the PTFE. Then, a smooth wipe already removes a measurable amount of such emitters, either due to mechanical effects or to chemical etching. Afterwards, polonium remains in the bulk of the sample, shielded from the cleaning agent. This means that a constant activity level is reached and that the procedures no longer prove very effective, as figure 3.17 shows. Moreover, side 'b' shows a high fluctuation of polonium activity more significant than the effect of the cleaning itself. This supports the hypothesis that the treatments cease to be effective once the surface has been removed: At that stage, the measured activity varies from one region of the disc to another (inhomogeneous loading) but, in contrast, the procedures barely make a change.

If the alpha-emitters migrated to the bulk, the shape of the peak in the spectrum would be affected as the alphas would lose more energy on collisions with PTFE molecules on the exit, thus contributing to the tail of the peak. A further study on this respect was carried out and is detailed in section 3.5.

Disc 2 A second sample, labeled '2', was similarly treated to check the reproducibility of the measurements. Figure 3.18 collects the resulting reduction factors. This time, a repetition of the ethanol wipe was carried out instead of the weak nitric acid procedure, in order to check whether it led to further reduction. In this case, side a was more efficiently loaded by a factor 2.87 ± 0.15 with respect to side '*b*'.

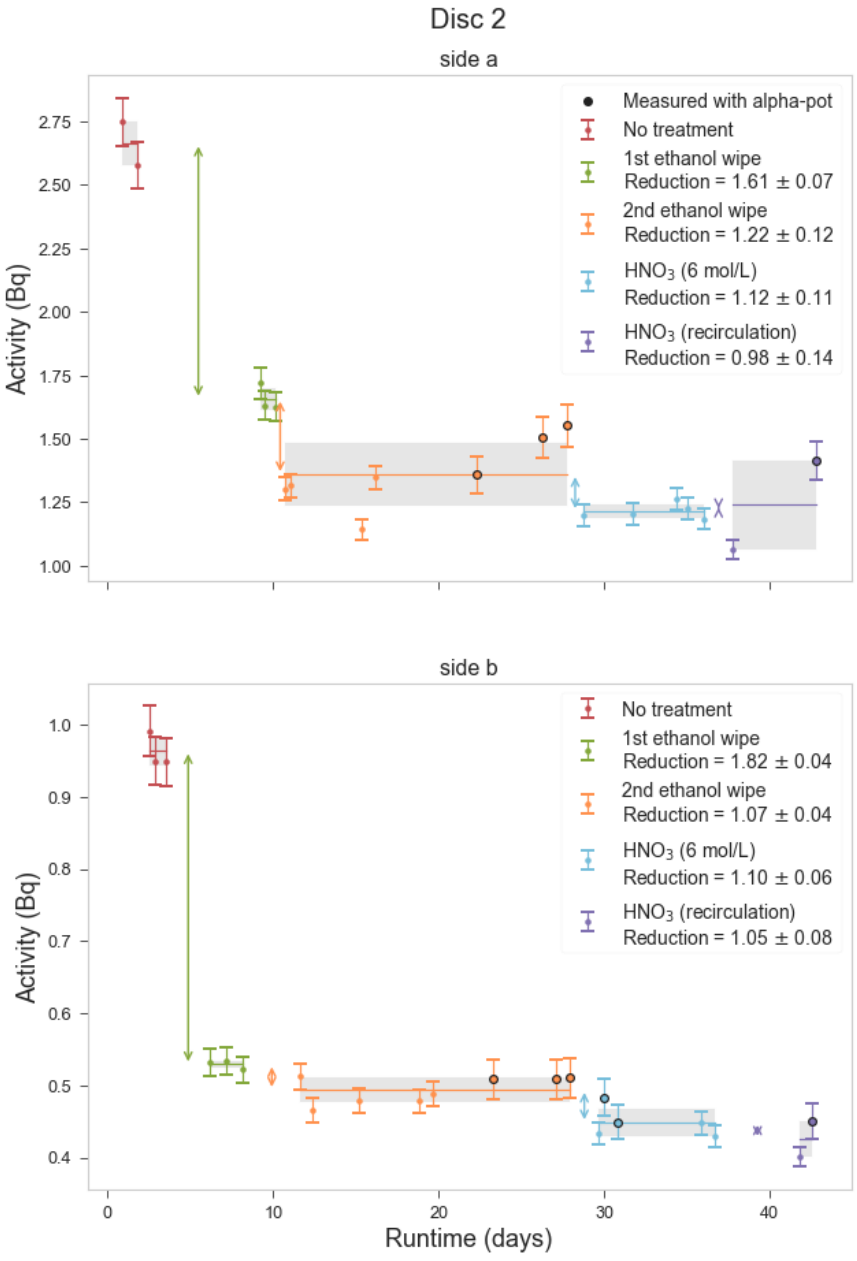

Figure 3.18: Cleaning procedures results on disc 2. In this case no fit correction was applied for the first treatment given the limited statistics previous to it.

Here again a constant level is hit after most surface contamination has been removed. This saturation effect is more evident in side '*b*', as it was the case with disc 1 too. The reduction factors are small but compatible for both sides, as well as the overall reduction from all the procedures. The saturation level differs on each side by a relative factor of 3. This might be an indication that the emitters do not come from the same depth level. If this were the case, the same saturation activity would be visible on either side of the disc. The discrepancy then implies that polonium sits on different layers closer to the surface. This hypothesis is supported by a shape analysis, as discussed in section 3.5.

The recirculated HNO_3 procedure was tested in order to see the impact of readsorption of polonium back onto the sample's surface. The result of this procedure proves that such effect was not significant, at that stage of our cleaning sequence. However, this effect might have been more apparent at the early stages, when the surface was more populated. In that case polonium could be dissolved in the acid and redeposited whereas, if barely any polonium was dissolved to begin with, not much readsorption should be expected. We want to investigate this in the future.

Disc 3 The ethanol wipe treatments have so far proved quite effective compared to the subsequent procedures. They were always applied first to the sample, when most of the emitters still sat on the disc surface. Further wiping led to polonium concentration decrease, as the measurements of disc 2 show. This means that the first wipe had left a considerable amount of polonium on the sample. From this information we can conclude that, albeit its removal efficiency is limited, ethanol solves polonium attached to PTFE to a certain level. Nevertheless, since the procedure involved wiping the PTFE with some tissue, the effect of polonium removal might have been due to the rubbing. Thus caused by a mechanical "etching" rather than chemical. Moreover, wiping as a cleaning procedure has no practical application for PTFE in XENON, as it could alter its surface structure and hence affect its reflectivity properties.

For such reason another procedure involving ethanol was tested on a third sample. Instead of rubbing the sample with cloth, it was simply left in an ethanol bath for some 15-20 minutes. This was the procedure referred as "ethanol dip" in section 3.3.4. The idea is to isolate the chemical effect of ethanol from any other effects related to the wiping.

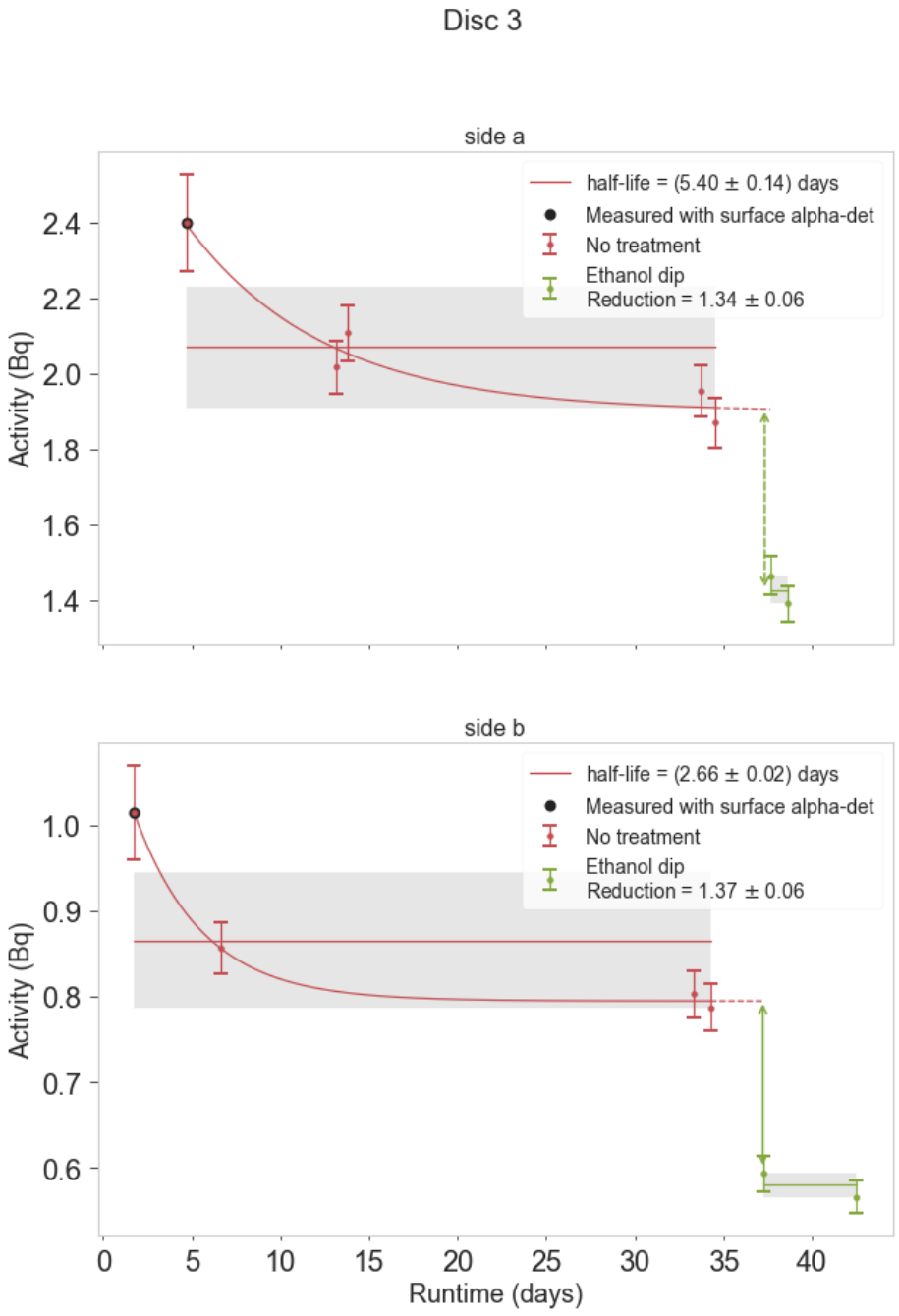

Figure 3.19: Ethanol dip result on disc 3.

Figure 3.19 depicts this procedure on disc 3. Similarly as for the case of the two ethanol wipes applied on disc 2, the reduction factors of this procedure on both sides coincide within the uncertainty. The cleaning yielded a reduction factor of 1.34 ± 0.06 for side 'a' and of 1.36 ± 0.06 for side 'b'. The first ethanol wipes led to factors of 1.57 ± 0.08 for side 'a' of disc 1 and of 1.61 ± 0.07 and

1.82 ± 0.04 for sides 'a' and 'b' of disc 2, respectively. Comparing these results, one can conclude that the mechanical effect of the wipe is negligible compared to the chemical etching effect. The ethanol dip procedure led to slightly lower removal factors, being the discrepancies probably linked to the absence of etching.

Disc 4 Another sample was again treated with the strong nitric acid solution as a first procedure, instead of the ethanol wiping. The aim was to determine the effect of the nitric acid alone on an untreated sample.

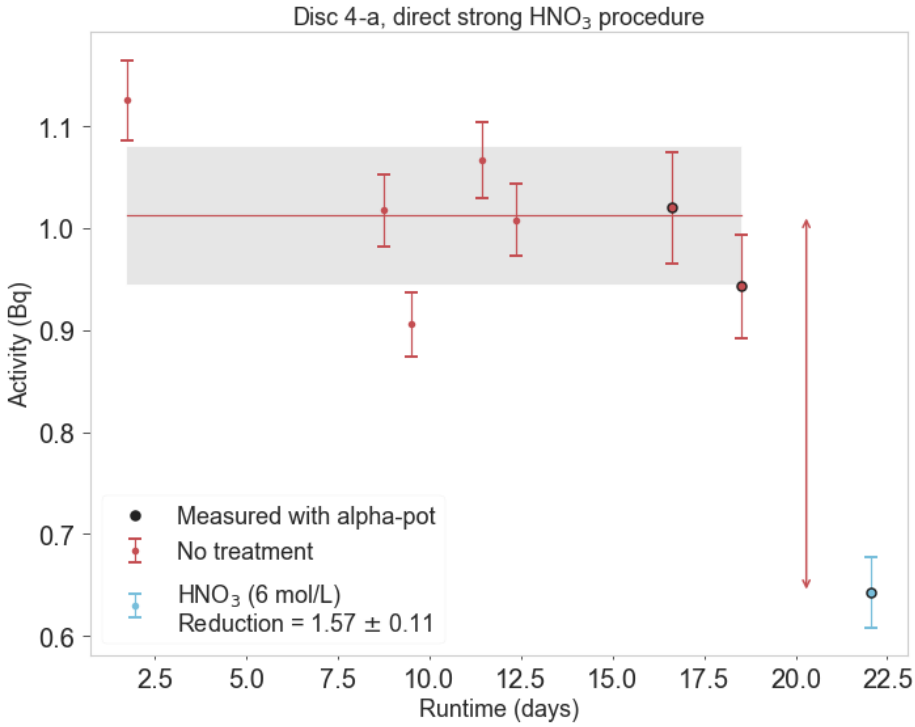

Figure 3.20: HNO_3 procedure result as initially applied on disc 4.

The reduction was not greater than that achieved by the initial ethanol wiping, as figure 3.20 shows: A factor of 1.57 ± 0.11, compared to a maximum reduction factor reached by ethanol of about 1.8. This result leads to an important conclusion: nitric acid is not a more efficient solver of polonium than ethanol. However, the measurement must be repeated to confirm this as this result on the reduction factor relies on a single post-treatment measurement. The time spent by the sample in the acid solution cannot play an important role either, given that the immersion in the acid was at least four times longer than in ethanol.

Summary of surface treatment results Table 2 gathers all the reduction factors obtained from the previous analysis. The overall reduction factor, after all the procedures that each disc

underwent, is also listed in the last column of the tables.

Table 2: Reduction factors of ^{210}Po cleaning procedures

	Disc 1-a	Disc 1-b	Disc 2-a	Disc 2-b
1st ethanol wipe	1.57 ± 0.08	-	1.61 ± 0.07	1.82 ± 0.04
2nd ethanol wipe	-	-	1.22 ± 0.12	1.07 ± 0.04
HNO_3 (5% mass)	1.24 ± 0.06	1.4 ± 0.15	-	-
HNO_3 (6 mol/L)	1.16 ± 0.05	1.09 ± 0.15	1.12 ± 0.11	1.1 ± 0.06
HNO_3 (60°)	1.06 ± 0.02	0.94 ± 0.09	-	-
HNO_3 (recirculation)	-	-	0.98 ± 0.14	1.05 ± 0.08
Total reduction	2.4 ± 0.1	1.44 ± 0.08	2.15 ± 0.31	2.26 ± 0.14

	Disc 3-a	Disc 3-b	Disc 4-a
Ethanol dip	1.34 ± 0.06	1.37 ± 0.06	-
HNO_3 (6 mol/L)	-	-	1.57 ± 0.11
Total reduction	1.34 ± 0.06	1.37 ± 0.14	1.57 ± 0.11

3.4 ^{210}Pb removal

In this section, the contribution from ^{210}Pb to the samples's activity is inferred as well as its reduction through the cleaning procedures. Given the long half-life of lead (22.3 years) compared to its daughters', we can assume initial equilibrium with the subsequent isotopes in the chain, ^{210}Bi and ^{210}Po.

Figure 3.21 illustrates this effect. The measured activity of polonium on disc 2 is arranged, as in figure 3.18, only this time the total time elapsed between the beginning of each measurement is displayed on the x-axis. During this time the sample was not only exposed to vacuum, as it was for the runtime in the abscissa of figure 3.18, but also to air, when it was stored outside of the detector. During the long (2-3 months) phase, after the sample was treated with the ethanol wipe for the second time, if only polonium were left in the sample, its activity would have followed the decay indicated by the black broken line. Instead, a gentle, positive slope reveals that lead is still present in the sample, leading to a rise in polonium activity.

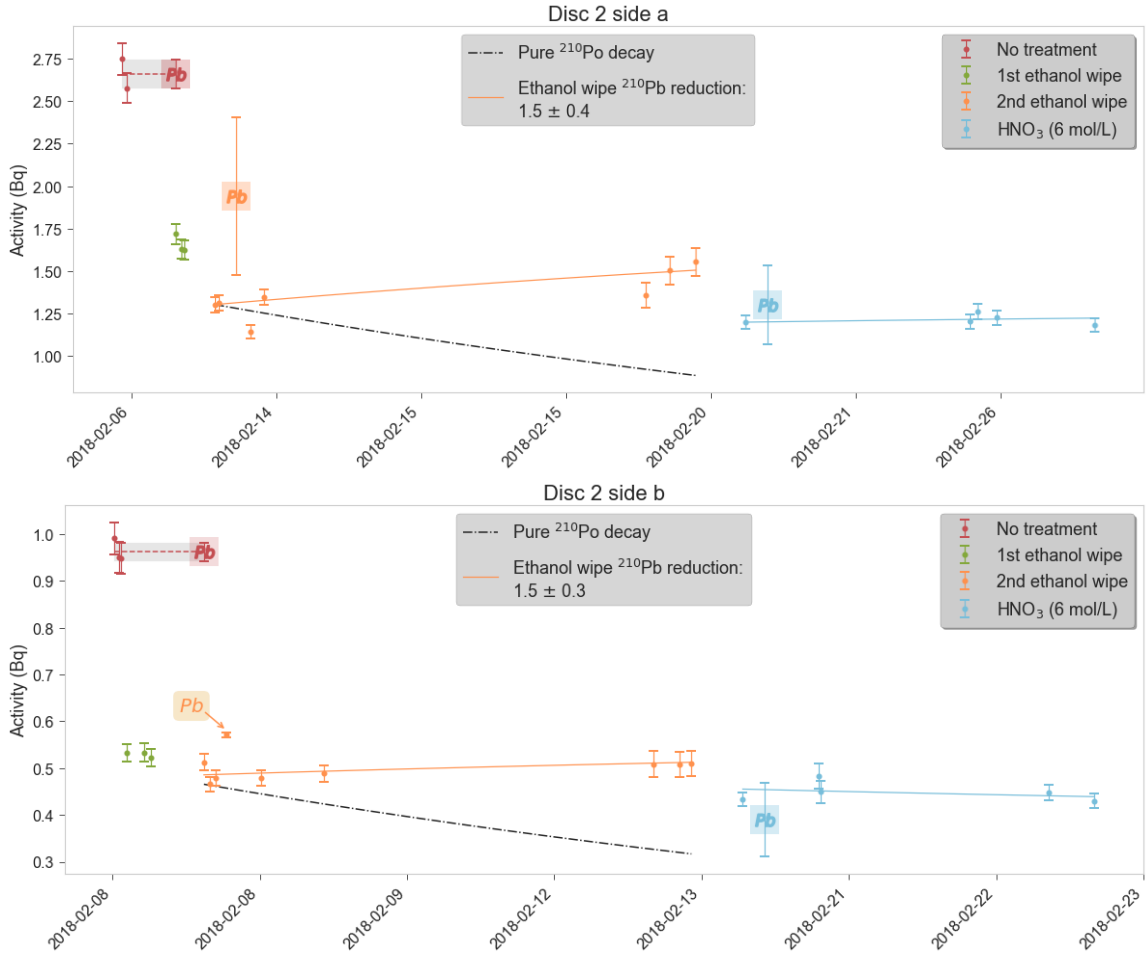

Figure 3.21: ^{210}Pb contribution to the activity in sample 2. Pure ^{210}Po decay trend included for comparison.

Such increase allows us to estimate the activity of lead after applying a procedure by fitting the evolution of polonium activity. The activity of ^{210}Po as a function of time can be calculated from Bateman's equations. If we neglect the contribution of the intermediate daughter ^{210}Bi ($\tau_{1/2} = 5$ days), and we assume a different initial concentration of lead and polonium, $A_{\mathrm{Pb}}(0)$ and $A_{\mathrm{Po}}(0)$, we obtain:

$$A_{\mathrm{Po}}(t) = A_{\mathrm{Po}}(0)e^{-\lambda_{\mathrm{Po}}t} + A_{\mathrm{Pb}}(0)\frac{\lambda_{\mathrm{Po}}}{\lambda_{\mathrm{Po}} - \lambda_{\mathrm{Pb}}}\left[e^{-\lambda_{\mathrm{Pb}}t} - e^{-\lambda_{\mathrm{Po}}t}\right] \tag{3.5}$$

and

$$A_{\mathrm{Pb}}(t) = A_{\mathrm{Pb}}(0)e^{-\lambda_{\mathrm{Pb}}t} \approx A_{\mathrm{Pb}}(0)$$

for $t \ll 1/\lambda_{\mathrm{Pb}}$, respectively. We used here the decay constants of ^{210}Pb and ^{210}Po, $\lambda_{\mathrm{Pb}} = 9.9 \cdot 10^{-10}\mathrm{s}^{-1}$ and $\lambda_{\mathrm{Po}} = 5.8 \cdot 10^{-8}\mathrm{s}^{-1}$. Neglecting the contribution of ^{210}Bi implies an error of ∼2%. The fit is performed by minimizing the function

$$\left(A_{\mathrm{Po}}(\Delta t) - A_{\mathrm{Po}}^{\mathrm{exp}}\right)^2 / \delta A_{\mathrm{Po}},$$

with $A_{\mathrm{Po}}(0), A_{\mathrm{Po}}^{\mathrm{exp}}$ and Δt fixed from the data. The only free parameter in the fit is $A_{\mathrm{Pb}}(0) \equiv A_{\mathrm{Pb}}^{\mathrm{post}}$. This parameter corresponds to the lead concentration right after carrying out the procedure and it is highlighted in the figure with a matching marker. The activity value of lead before treating the sample, $A_{\mathrm{Pb}}^{\mathrm{pre}}$, is assumed to coincide with the average of polonium at that phase (equilibrium condition). Lead can also be desorpted, as we will see in section 4.5, where evaporation of ^{212}Pb is discussed. However, the effect is negligible. Then, the reduction factor of the second ethanol wipe is estimated as

$$R_{\mathrm{F}} = \frac{A_{\mathrm{Pb}}^{\mathrm{pre}}}{A_{\mathrm{Pb}}^{\mathrm{post}}}.$$

The removal from the first ethanol wipe was neglected here, as that stage did not last long enough to see a significant evolution of polonium activity.

Applying this same algorithm to side *a* of disc 1, we obtained further results for ^{210}Pb. Those results are sketched in figure 3.22. In this case, the ethanol wipe stage lasted long enough so that the lead activity could be estimated, although with great uncertainty so it was not taken into account for the reduction factor calculation. This calculation was performed in this occasion for the weak HNO_3 procedure and the initial activity of lead was again assumed to coincide with that of polonium at the untreated stage. Table 3 summarizes the reduction factors of ^{210}Pb inferred by this method.

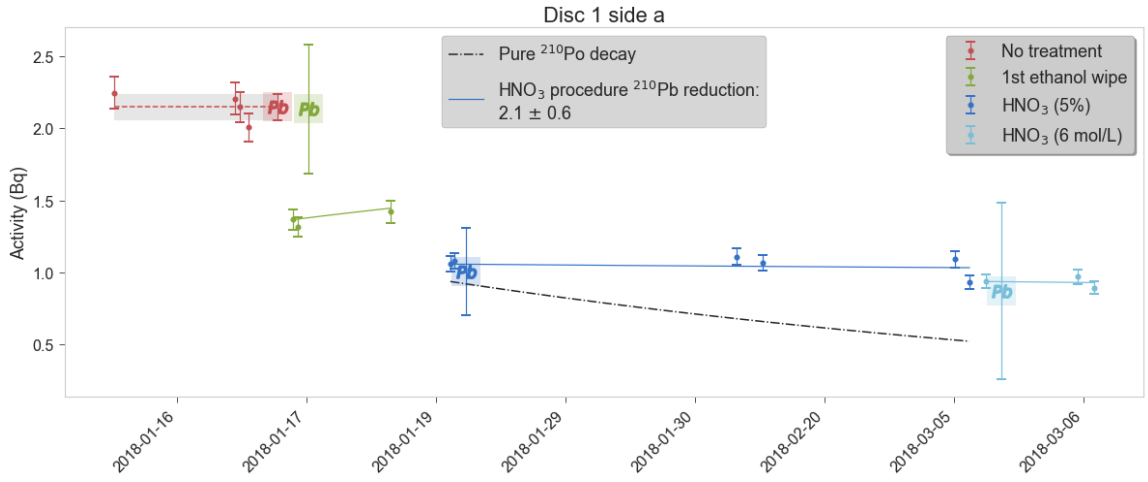

Figure 3.22: ^{210}Pb contribution to the activity in sample 1 side *a*.

Table 3: Reduction factors of ^{210}Pb cleaning procedures.

	Disc 2-a	Disc 2-b	Disc 1-a
Ethanol wipe	1.5 ± 0.4	1.5 ± 0.3	-
HNO_3 (5 %)	-	-	2.1 ± 0.6

3.5 Peak shape analysis

In order to explain the decreasing efficiency of the consecutive cleaning procedures applied on a sample, the distinction between events coming from the surface and from the material bulk was put forth. Once most events were removed from the surface, polonium is mainly present inside the bulk. There, even strong lead solvents like nitric acid cannot remove much of the remaining activity. Hence, the activity leveled off.

In order to test this hypothesis, an analysis of the evolution of the peak shape was carried out. A major migration of the emitters to the deep bulk of the substrate would be reflected in a swelling of the peak's left tail. the energy of the alphas would be more likely to be lost in collisions with PTFE molecules and any other impurity (for example dust). As a matter of fact, this could be seen in a set of measurements of disc 1 after the strong HNO_3 was applied. Figure 3.23 shows it.

The first condition to compare different peaks was to have them following a distribution centered in the same energy channel. This was not always the case even when measuring the same α-decay, due to some changes in the electronics of the setup. This would result in a shift in the channels. However, the calibration linearity was always fulfilled so the central channels were shifted to coincide with a fixed established value when they differed. Only data recorded by RaMon was used for this study. Afterwards, an initial set of measurements from the untreated state of the sample was taken as reference and all the statistics belonging to this set were combined and normalized. Then, all the individual peaks after the subsequent procedures were normalized and overlapped with this reference peak. Figure 3.23 demonstrates some of these overlapped spectra. A slight discrepancy is already visible in the figure, with a smearing of a few channels of the blue peak with respect to the reference (red).

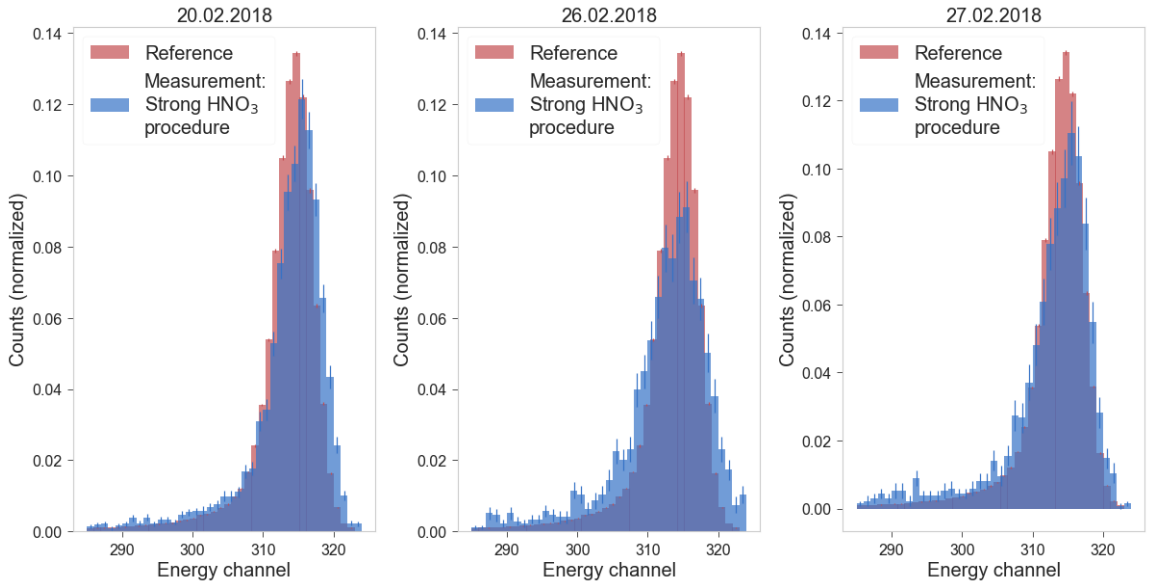

Figure 3.23: Instance of the overlapping process of the peaks of the processed sample with the initial state.

For each energy channel (each bin, labeled i), the residuals in the counting content (n_i)were was computed as its ratio with the reference: n_i/n_i^{ref}. Finally, this ratio was normalized to the total number of compared measurements, so that if the shape of the peak had not varied at all, the spectrum would follow a constant distribution around one.

As an initial cross-check, this analysis was carried out for the reference measurement. Figure 3.24 shows that the peak was not deformed during the initial phase. Indeed, when comparing all the statistics of this stage to the very first run of the set, the distribution of residuals in the counting content of the bins is very well described by a constant compatible with one.

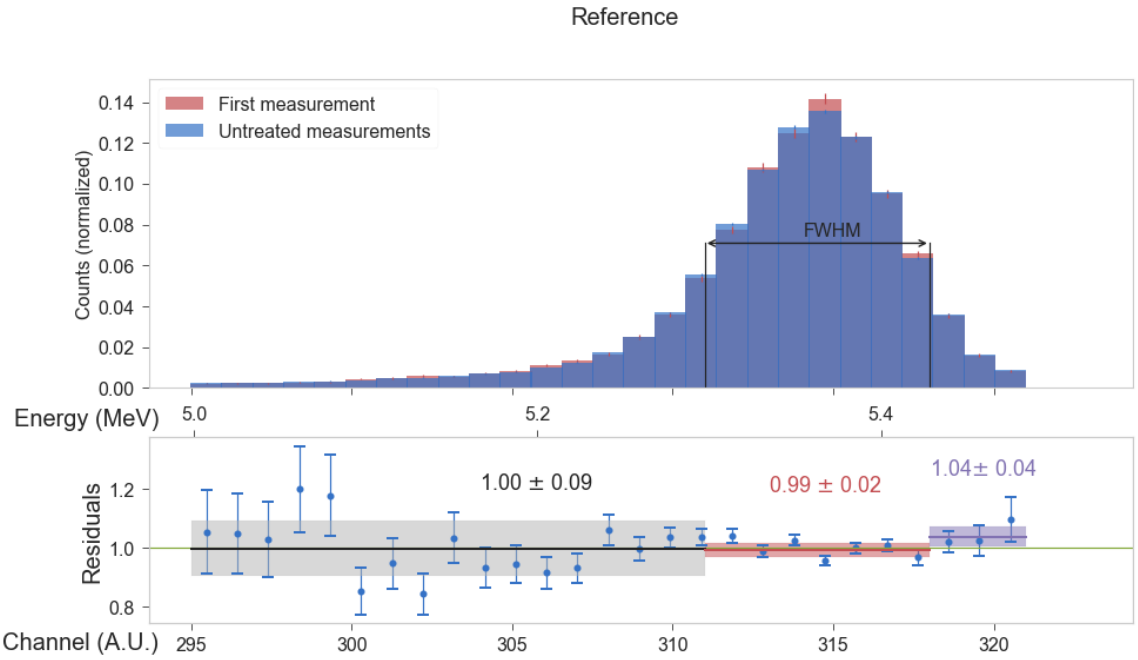

Figure 3.24: Proof of concept of the shape analysis. Stability of the shape during the initial stage.

Once the analysis was tested and the reference shape was proved to be stable, the deformation caused by the treatments was estimated as follows: The distribution of the residuals was plotted for the combined set of measurements after all the treatments, as figure 3.25 gathers. Then, the full width at half maximum (FWHM) interval of the peak was computed and three additional averages of the deviations were determined: the average in the FWHM (red line), in the interval up to its lower limit (left tail, black line) and in the interval from its higher limit (right tail, purple line). By comparing these values, the migration of polonium to the tails can be roughly quantified. Indeed, as the figure exposes, the average on the left tail exceeds that on the FWHM; reflecting how, in comparison with the original state, the left tailed swelled when the treatments were applied. This is already visible in the top graph, where the overlapped peak (blue) clearly exceeds the reference for channels 305-310. The opposite is true on the right tail, implying that the most energetic depositions (surface events) are less likely to happen when after the sample has been treated.

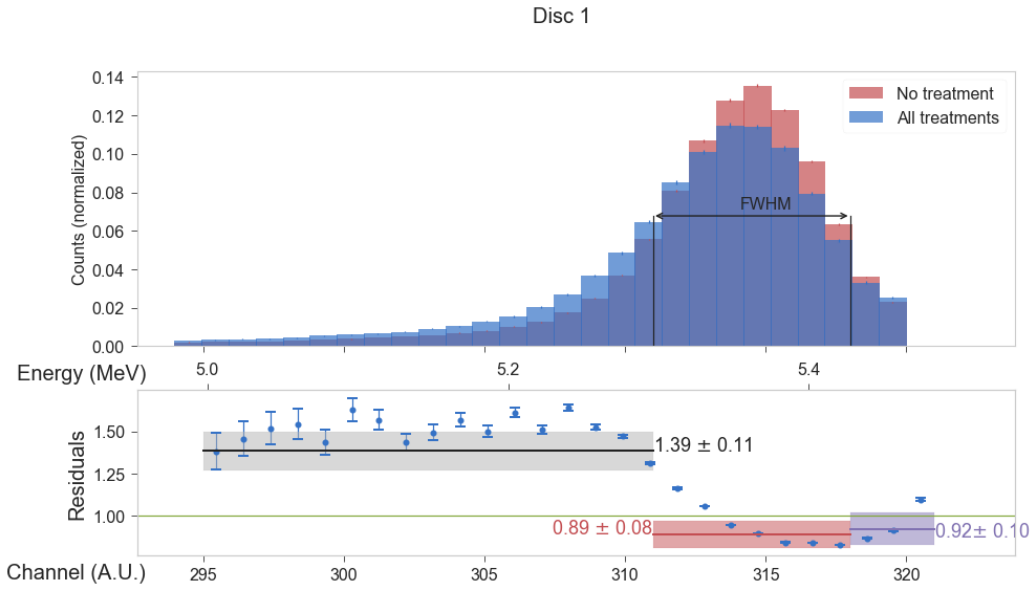

Figure 3.25: Shape analysis result after all cleaning procedures and either side of disc 1.

Similar results as above were found when performing the same analysis on each separate side of the disc. Thus, the migration affects equally to both sides.

The same analysis was performed for side 2, leading to very similar results, assuring reproducibility of this effect. As a conclusion, polonium either migrated to the inner layers of the PTFE bulk after the surface was cleaned, or it had already been diffused there. This last hypothesis will be argued in the following chapter, particularly in the subsection dedicated to a similar shape analysis as the one exposed here. There, a comparison with the much shorter-lived ^{212}Bi is provided.

3.6 Conclusion

In this section we described the experimental setup and measurement procedure to test the cleaning efficiency of different surface treatments. The reduction factors of ^{210}Po and ^{210}Pb are given in tables 2 and 3 respectively. The time evolution of ^{210}Po activity during several months allowed for a tracing of the ^{210}Pb activity, as explained in section 3.4. We investigated the cause of the limited removal efficiency for the tested procedures in terms of an analysis of the ^{210}Po peak shape. This led us to the conclusion that this isotope migrated to the inner layers of the PTFE, probably by diffusion effects or by the recoil momentum when undergoing α-decay.

Lastly, evaporation of ^{210}Po was detected on several samples. This entailed an activity decrease trend which was accounted for when computing the reduction factors of the cleaning procedures. It also contributed to an increase in the background activity of the alpha-spectrometer (RaMon), as commented in section 3.3.2.

4 Removal of ^{212}Pb

4.1 Motivation

The removal of ^{210}Po by means of surface cleaning was discussed in the previous section. We saw that the presence of ^{210}Pb played an important role in the evolution of ^{210}Po concentration. In section 2 we saw the gravity for the XENON experiment of ^{210}Pb. In the light of this, a further study on the removal of lead, rather than polonium, was additionally conducted and it is outlined in this section.

In order to investigate the cleaning efficiency of lead from PTFE, an isotope of this element is needed whose decay signal could be recorded using the detectors described in this work and with a reasonable half-life. The isotope chosen for the study was the beta-emitter ^{212}Pb, since it has a relatively short half-life, 10.6 hours. This way background introduced in the spectrometers is minimized, as opposed to using, for example ^{210}Po.

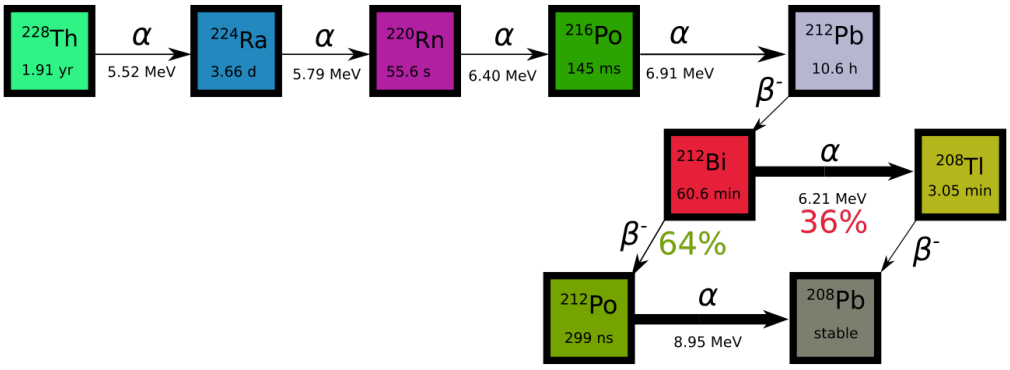

Figure 4.1: ^{228}Th decay sub-chain, from ^{232}Th series.

Indirect detection of ^{212}Pb is possible using our alpha spectrometers. Figure 4.1 shows an excerpt of the decay chain of ^{232}Th containing ^{212}Pb. ^{212}Pb undergoes beta decay, undetected by the PIN diode. However, its daughter ^{212} Bi is an alpha emitter. The half-life of ^{212}Bi is 61 minutes much shorter than the 10.6 hours half-life of ^{212}Pb. Therefore, ^{212}Bi follows, to a good approximation, a decay law with the half-life of ^{212}Pb, allowing for the tracing of lead.

4.2 Sample loading

For this investigation, identical PTFE samples as for the polonium removal study were used (see figure 3.9). The loading method was based on a recirculation setup similar to the one exposed in section 3.3.1. Figure 4.2 displays this loading setup. It features a ^{228}Th source of $\sim$ 10 kBq of strength. ^{228}Th is in equilibrium with ^{224}Ra, which decays to ^{220}Rn. ^{220}Rn, commonly referred to as 'Thoron' emanates in the vessel and is then flushed through a filter into the sample vessel, where the PTFE samples sit. Thoron plates-out its daughters, ^{216}Po and ^{212}Pb, onto the PTFE. The half-lives of ^{220}Rn and ^{216}Po are in the scale of seconds, negligible compared to the 10.6 hours of ^{212}Pb. The latter dictates the time scale of the loading phase. Usually, the samples were loaded for 5 to 7 days, so that the ^{212}Pb reaches its full saturation level. Once the loading is set to finish and the valves are closed to interrupt the recirculation, the sample is left inside the vessel for one or two hours to ensure that all the thoron has decayed away ($\tau_{\mathrm{Rn220}} = 55$ s), before proceeding to its extraction. This is done fore safety reasons.

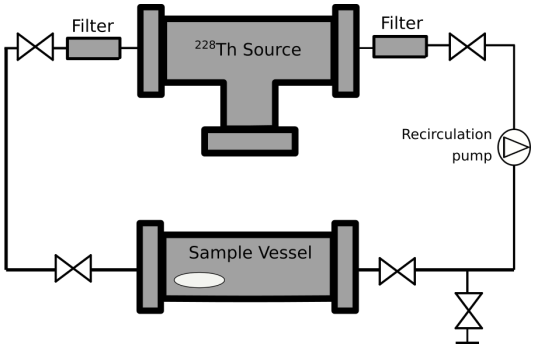

Figure 4.2: ^{220}Rn-loading setup.

Only one side of the disc was measured in this case, so the disc was simply set on the vessel wall. The chosen side to measure was the one which faced the air inside the vessel, parallel to the gas flow.

4.3 Tested cleaning procedures

Before describing the measurement technique, we list here the treatments which were tested. Many of them are common to the ones tested for ^{210}Po so that their efficiency on removing the different isotopes can be compared.

1. **Water dip:** Immersion in ultra pure water (UPW) for 30 minutes.
2. **Ethanol dip:** Bath in ethanol for 30 minutes.
3. **Weak nitric acid procedure:**
   (a) Immersion of the sample in 5% (by mass) HNO_3 dissolved in ultra pure water (UPW).
   (b) Sonication for 15 minutes. Then the sample is left in the bath for 2 hours.
   (c) Rinsing with de-ionized water.
   (d) Drying by blowing nitrogen.
4. **Strong nitric acid procedure:** Variation of the weak nitric acid procedure, using a HNO_3 solution of 6 mol/L (32%).

5. **Acetic acid procedure:**

   (a) Immersion in a 1% (by mass) acetic acid (CH_3CO_2) solution for 5 minutes.

   (b) Immersion in a 1% nitric acid and 3% hydrogen peroxide (H_2O_2) solution for 5 minutes

   (c) Immerse the disc in another glass with a fresh acetic acid solution for 5 minutes.

   (d) Immerse the disc in another glass with a fresh nitric acid and hydrogen peroxide solution for 5 minutes.

   (e) Rinsing with de-ionized water.

   (f) Drying by nitrogen blowing.

4.4 Measurement procedure

Once the samples were loaded with ^{212}Pb and extracted from the loading setup, they were inserted in the surface alpha-detector (RaMon was no longer used for this study). An example of measured energy spectrum is depicted in figure 4.3. The two peaks correspond to the alphas emitted by ^{212}Bi (red) and its daughter ,^{212}Po (green). As figure 4.1 illustrates, ^{212}Bi has two exclusive decay modes: alpha and beta, with branching ratios of 36% and 64% respectively. This branching ratios were found in the measurements and are shown in figure 4.3 as the total counts quotient between both peaks. For our analysis we monitor both branching ratios of ^{212}Bi by combining the counts in both peaks.

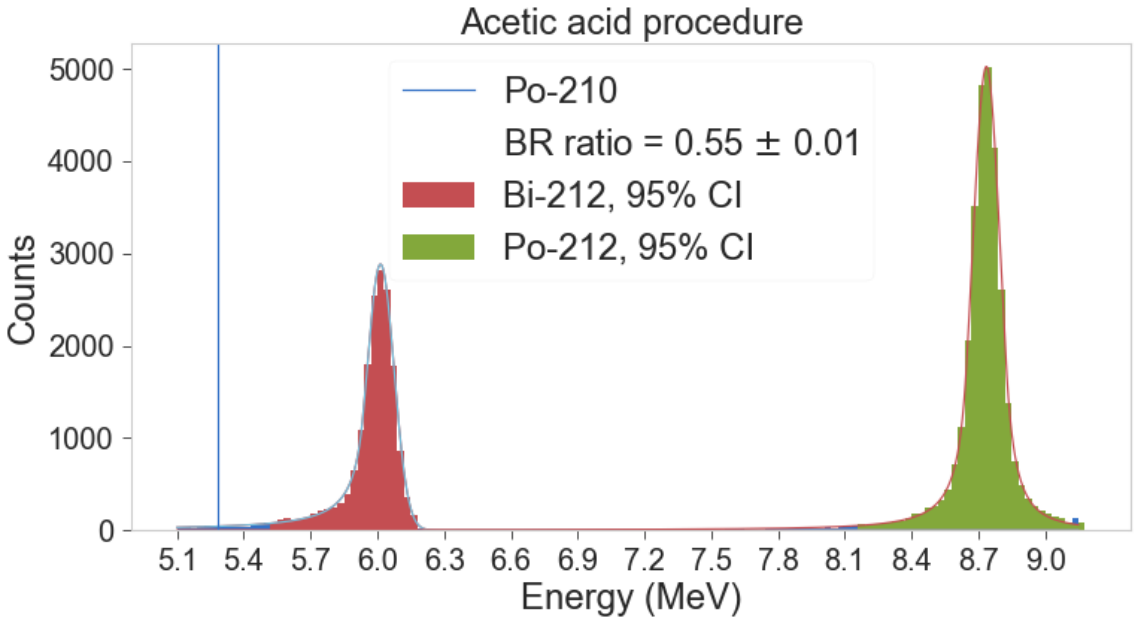

Figure 4.3: Spectrum obtained from a ^{212}Pb-loaded sample.

The detector still contained some background from ^{210}Po, as explained in section 3.3.2 and as indicated in the spectrum. Its peak, however, does not interfere with that of ^{212}Bi and it gets

cut for the posterior analysis. Other interesting feature of the spectra is the right tail of ^{212}Po, corresponding to the energy deposited when bismuth undergoes alpha-beta decay [57]. This was modeled by a function consisting on a generalization of the crystalball, defined in (3.1), but with two tails, each with different exponents n_1 and n_2:

$$f(E;\mu,\alpha,\alpha,n_1,n_2,\sigma) = N \cdot \begin{cases} A_1 \cdot \left(B_1 - \frac{E-\mu}{\sigma}\right)^{-n_1}, & \text{for} \quad \frac{E-\mu}{\sigma} \leq -\alpha \\ \exp\left(-\frac{(E-\mu)^2}{2\sigma^2}\right), & \text{for} \quad \frac{E-\mu}{\sigma} > -\alpha \\ A_2 \cdot \left(B_2 - \frac{E+\mu}{\sigma}\right)^{-n_2}, & \text{for} \quad \frac{E+\mu}{\sigma} \geq +\alpha \end{cases}, \tag{4.1}$$

where

$$A_i = \left(\frac{n_i}{|\alpha|}\right)^n_i \exp\left(-\frac{|\alpha|^2}{2}\right),$$
$$B_i = \frac{n_i}{|\alpha|} - |\alpha|,$$

for i = 1,2.

4.4.1 Computation of reduction factors

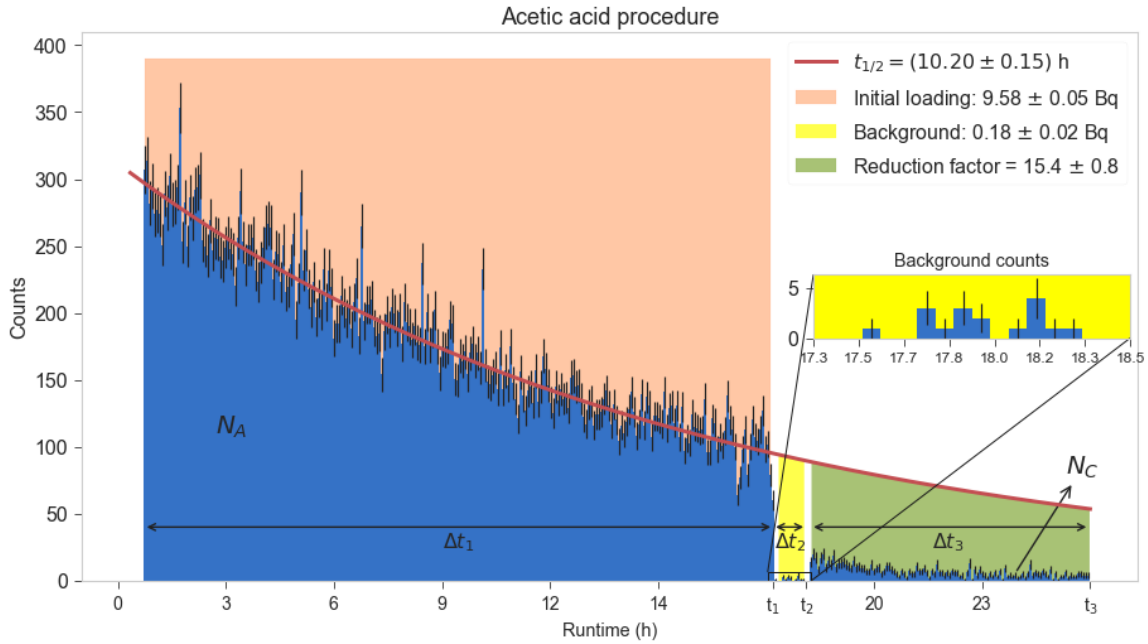

Figure 4.4: Time evolution of the ^{212}Bi events throughout the measurement.

Figure 4.4 shows an exemplar measurement of ^{212}Pb reduction after a cleaning procedure (with acetic acid). Three different regions can be distinguished in the figure:

1. The initial, orange interval (Δt_1) at which the loaded, untreated sample is measured (blank), with a total bismuth counting N_A. The evolution follows the decay of ^{212}Pb.

2. The intermediate, yellow interval (Δt_2) when the sample is undergoing the treatment and the detector background is measured (over the same energy interval as before), with total background counting N_B.

3. The last, green interval (Δt_3) when the treated sample is again measured with an integral bismuth counting N_C.

The background events cannot be related to ^{210}Po, since these energy channels are rejected from the beginning. Most likely, the lead gets desorpted from the PTFE surface into vacuum and then attached to the diode. Such effect would imitate the result obtained already for ^{210}Po discussed in section 3.3.3. Lastly, the surface of the sample tray itself facing directly the diode and which is in direct contact with the loaded samples is also covered using an uncontaminated PTFE disc during the recording of the background, to imitate the measuring conditions. This way we rule out the tray surface as the source of the background.

The activities indicated in this section have been corrected for geometry efficiency. However, given that the detector employed and the sample-diode distance were always the same, this correction factors out in the calculation of the reduction factors.

We carried out two complementary analysis to compute the reduction factors and we outline them below:

Analysis 1: total counts The green region in figure 4.4 reaches up to the fit line in order to visually illustrate the missing signal area due to the reduction by the cleaning. The reduction factor is computed as:

$$R_1 = \frac{A_0^A}{A_0^C} = \frac{N'_A}{N'_C}\frac{e^{\lambda t_2} - e^{\lambda t_3}}{e^{\lambda t_0} - e^{\lambda t_1}}. \tag{4.2}$$

where $\lambda \equiv \lambda_{\mathrm{Pb212}} = 235.4\ \mathrm{s}^{-1}$ is the decay constant of ^{212}Pb; A_0^A stands for the initial activity of the untreated sample and A_0^C for the activity of the clean sample at the same time point. We obtain these quantities from the total number of counts, N'_A and N'_C, acquired during Δt_1 and Δt_3 respectively, by considering the integrals:

$$N_A = \sum_{t<t_1} n_{A,i} = \int_{t_0}^{t_1} A_0^A e^{-\lambda t'}\,\mathrm{d}t' = \frac{A_0^A}{\lambda}\left[e^{\lambda t_0} - e^{\lambda t_1}\right], \tag{4.3a}$$

$$N_C = \sum_{t>t_2} n_{C,i} = \int_{t_2}^{t_3} A_0^C e^{-\lambda t'}\,\mathrm{d}t' = \frac{A_0^C}{\lambda}\left[e^{\lambda t_2} - e^{\lambda t_3}\right], \tag{4.3b}$$

and then correcting by subtracting background counts:

$$N'_A = N_A - N_1^B, \tag{4.4a}$$

$$N'_C = N_C - N_3^B. \tag{4.4b}$$

Here N_i^B (i = 1,3) stands for number of background counts during Δt_i. These amounts are extrapolated from the measured background counts, N_2^B, during Δt_2: First, we compute A_0^B at t_1, as in equations (4.3):

$$N_2^B = \int_{t_1}^{t_2} A_0^B e^{-\lambda t'} \mathrm{d}t' = \frac{A_0^B}{\lambda} \left[e^{-\lambda t_1} - e^{-\lambda t_2} \right],$$

and then the expected number of counts during Δt_0 and Δt_3:

$$N_3^B = \int_{t_2}^{t_3} A_0^B e^{-\lambda t'} \mathrm{d}t' = \frac{A_0^B}{\lambda} \left[e^{-\lambda t_2} - e^{-\lambda t_3} \right] = N_2^B \frac{e^{-\lambda t_2} - e^{-\lambda t_3}}{e^{-\lambda t_1} - e^{-\lambda t_2}}, \tag{4.5a}$$

$$N_1^B = \int_{t_0}^{t_1} A_0^B e^{-\lambda t'} \mathrm{d}t' = N_2^B \frac{e^{-\lambda t_0} - e^{-\lambda t_1}}{e^{-\lambda t_1} - e^{-\lambda t_2}}, \tag{4.5b}$$

All uncertainties of N_i are assumed to be poissonian.

Analysis 2: comparison to fitted line A second analysis based on the fitted decay function was also employed to double-check the results. In this case the measured counts during the clean stage, N'_C, was compared to the total counts we expected from the decay function, N'_E:

$$N_E = \int_{t_1}^{t_2} A_0^f e^{-\lambda_f (t')} \mathrm{d}t' = \frac{A_0^f}{\lambda_f} \left[e^{-\lambda_f t_2} - e^{-\lambda_f t_3} \right], \tag{4.6}$$

where the subscript f refers to fit parameter. Then we apply the background correction, $N'_E = N_E - N_3^B$, and the reduction factor is given by:

$$R_2 = \frac{N'_E}{N'_C}, \tag{4.7}$$

This method led to a more precise reduction factor than the counting analysis for the measurement of the strong nitric acid procedure, which for technical reasons, provided significantly less statistics. However the first analysis is preferred for its robustness and independence of fitting parameters.

4.5 Removal results

The measurement of the sample treated with the acetic acid procedure was exposed in figure 4.4. The rest of the procedures listed in section 4.3 led to the measurements gathered in figure 4.5. In the figure, only the reduction factors obtained by the first analysis are included. Table 4 collects the results from both methods.

Table 4: Reduction factors of ^{212}Pb cleaning procedures.

Procedure	Counting method	Fitting method
Acetic acid	11.8 ± 0.5	11.8 ± 0.6
HNO_3 (6 mol/L)	38.4 ± 12.2	30.1 ± 6.7
HNO_3 (5 %)	5.2 ± 0.3	5.2 ± 0.9
Ethanol dip	7.9 ± 0.2	7.5 ± 0.3
Water	3.05 ± 0.04	2.88 ± 0.07

Starting with the strong nitric acid procedure, its shorter duration led to limited statistics. Furthermore, at this point of the study, the background was overestimated: The surface of the tray in front of the diode, where the sample had been set, was not covered with a PTFE disc (as was the case of the following background measurements). This surface would not be recorded with the sample shielding it.

Regarding the water procedure, a sudden change of slope can be seen right after cleaning, which remains above of a second fitted exponential. This could reflect a more efficient removal of lead than of bismuth, thus the shorter half-life of the fit.

This study proves that nitric acid, on a high concentration, is an excellent solver of lead in PTFE, with a reduction factor larger than 25 to a 1-sigma confidence. On smaller concentrations it also removes efficiently a good amount of lead, as the result of the weaker (5%) HNO_3 procedure shows. It is also the case of the so-called acetic acid procedure, which also includes a solution of 1% HNO_3. By comparing the results of the latter to the former, we can conclude that, if such a weak (1%) solution of nitric acid is used, the main removal work is done by either the acetic acid (1%) or the hydrogen peroxide (3%). As we saw in the previous chapter, ethanol is also a effective solver, slightly more so than highly dissolved HNO_3. Additionally, ethanol is safer to handle. The reaction of these chemicals must be compared to the effect of an immersion in ultra pure water. This last result demonstrates that UPW removes a significant amount of lead from PTFE.

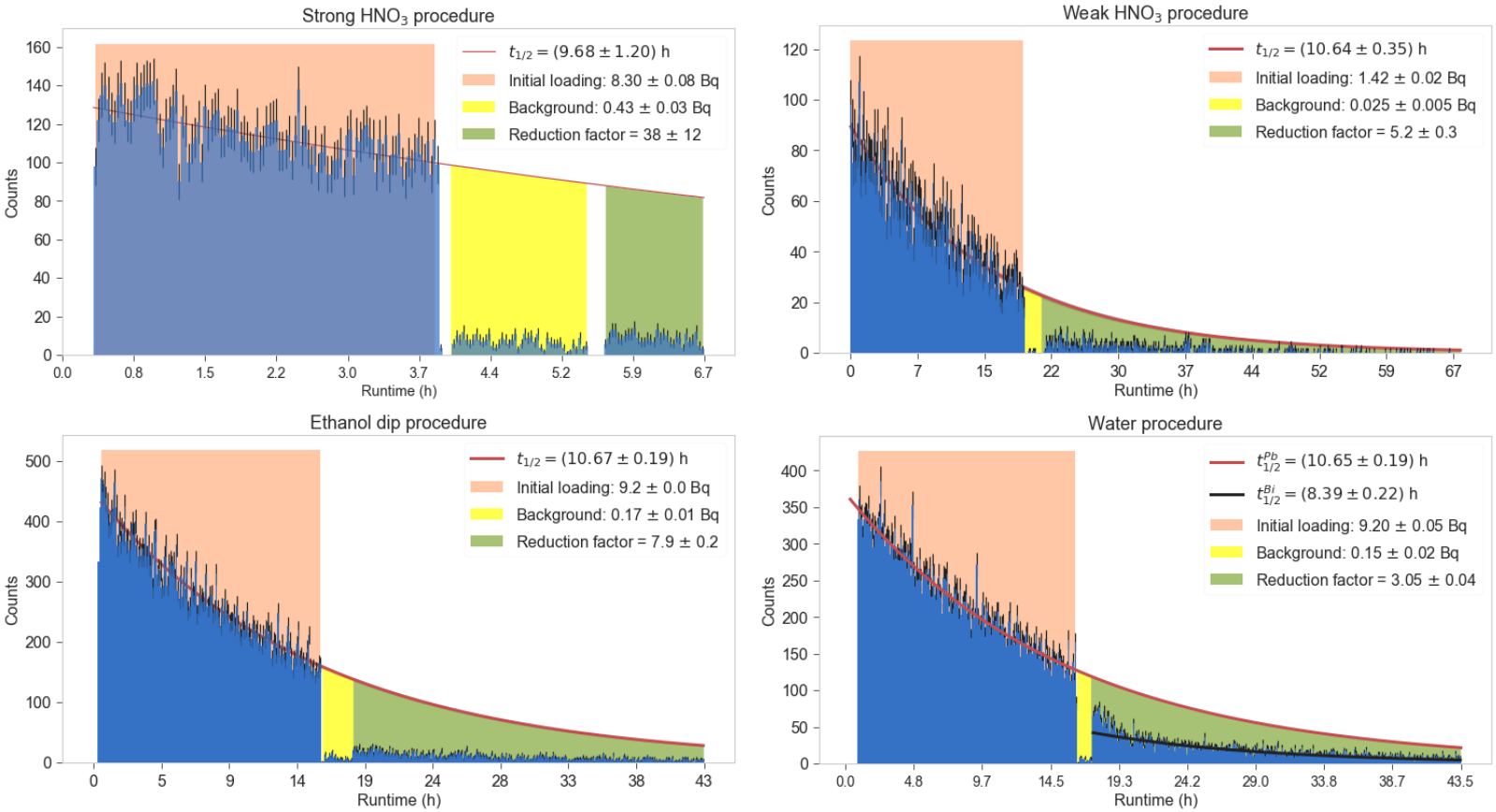

Figure 4.5: Removal of ^{212}Pb by means of different cleaning procedures.

In section 3.3.5 we outlined the reduction of ^{210}Po and ^{210}Pb. By comparison with the results collected in table 4.5, we see that ^{212}Pb is much more efficiently removed when comparing the same procedures. An explanation was offered based on the change of shape of the ^{210}Po peaks before and after the treatments: polonium could be relatively easily removed from the samples surface but once the bulk events became relevant, the procedures began to render unfruitful. The samples loaded with ^{210}Po had spent some years inside the loading setup, time enough for ^{222}Rn and its daughters to diffuse inside the PTFE and be shielded therein from the chemicals. On the other side, the samples studied in this chapter, loaded with ^{220}Rn, spent only some days, so the diffusion is not so evident.

The way to compare these diffusion effects is by carrying out again the shape analysis of the ^{212}Bi peaks, which is the aim of next section.

4.6 Shape analysis

The peaks of ^{212}Bi and ^{212}Po were also analyzed in terms of its shape variation following the steps outlined in section 3.5. Figures 4.6 and 4.7 collect the combined data of the peaks before and after the treatments as well as the distribution of the bin content residuals.

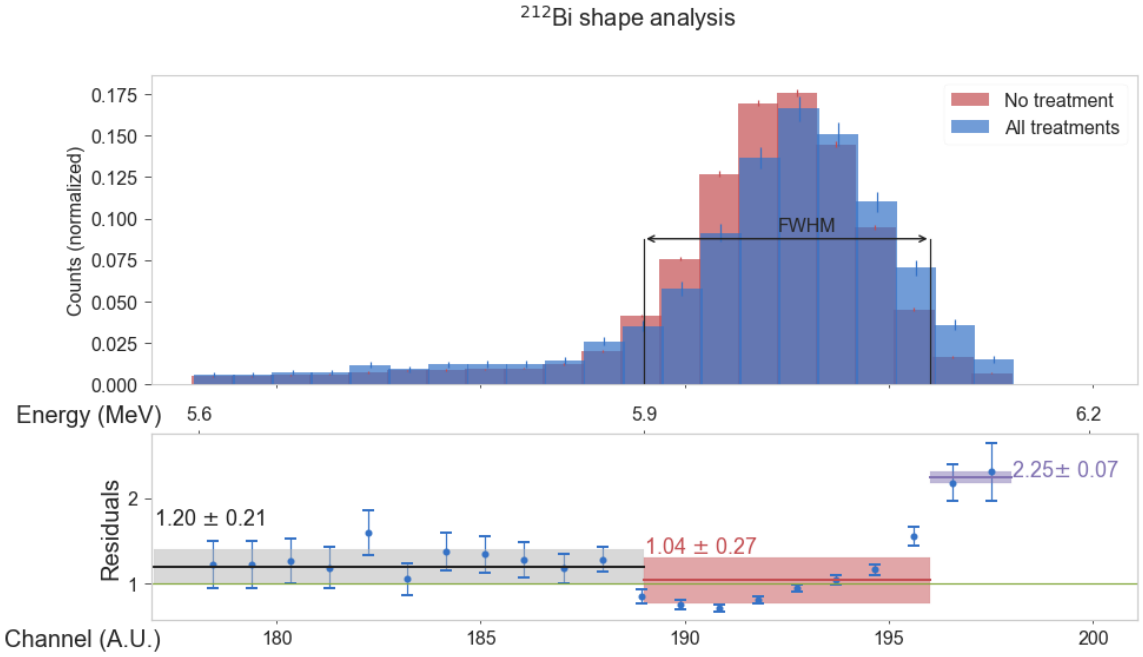

Figure 4.6: Shape analysis of the ^{212}Bi events before and after treatment.

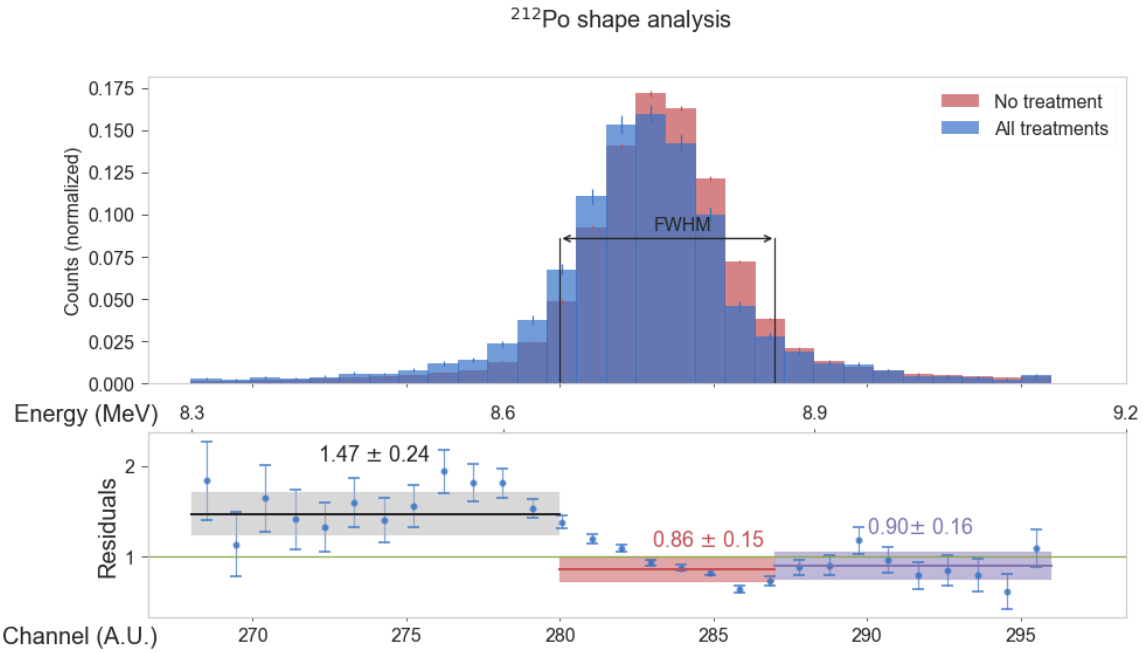

Figure 4.7: Shape analysis of the ^{212}Po events before and after treatment.

Table 5: Average residuals along the peak distributions.

	Disc 1 (^{210}Po)	Disc 2 (^{210}Po)	^{212}Bi results
Left tail	1.23 ± 0.09	1.34 ± 0.22	1.43 ± 0.25
FWHM	0.98 ± 0.05	0.93 ± 0.06	0.87 ± 0.12
Right tail	0.70 ± 0.06	0.74 ± 0.01	0.78 ± 0.19
Total	1.03 ± 0.20	1.02 ± 0.26	1.06 ± 0.33

Figure 4.6 features a very similar effect as the one depicted in section 3.5: The left tail residuals exceed the ones in the FWHM, which again hints to a migration of lead to the inner layers of the material, as shown in table 5. In the case of ^{212}Pb we started from a relatively higher surface concentration compared to ^{210}Po, which would have already diffused to the interior. Given that we are comparing the shape after the treatments here, bismuth was much more removed from the surface, as the reduction factors proved too. Therefore, the residuals in the FWHM are much lower with respect to the untreated state than in the case of ^{210}Po, where we initially had relatively less surface events to remove.

The comparison is even more evident in figure 4.8, where we overlap the combined data of treated ^{212}Bi samples and treated ^{210}Po. The mean channel of the latter were shifted to coincide with that of the former before analyzing it. In the figure, a very significant swelling of the ^{210}Po left tail can be noticed, specially in the part closer to the FWHM inferior limit (channels 185-190). The right

tail is also visibly higher. This spreading of the peak is expected for a source contained deeper in the material bulk, as anticipated.

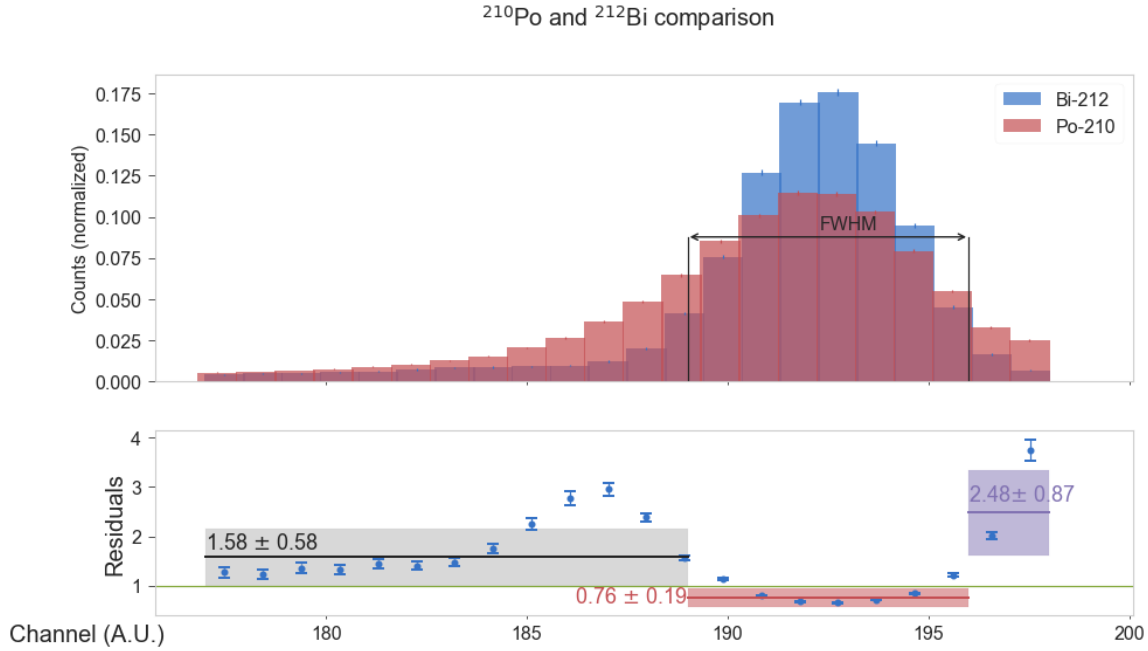

Figure 4.8: Comparison of ^{212}Bi and ^{210}Po shapes.

This comparison was only sensible taking ^{212}Bi as reference. ^{212}Po has a right tail produced by the alpha-beta decay depositions, as discussed in section 4.4, therefore the shape of the peak is completely different to that of ^{212}Bi.

Based on this analysis, the next logical step would be using the shape of the peaks to estimate the distribution of the emitters in the material. To do so, the interaction of polonium and bismuth with PTFE molecules in a determined depth range would be simulated. However, this simulation does not fall in the scope of this work.

4.7 Conclusion

In this section we compared quantitatively the efficiency of several surface treatment procedures on removing ^{212}Pb. Most of them were also identical to those detailed in section 3. We concluded that nitric acid procedure greatly reduces the population of ^{212}Pb in PTFE, especially in high concentrations. Other effective alternatives include ethanol and the acetic acid procedure. We want to remark that the latter does not only consist on acetic acid but also on a solution of 1% HNO_3 and 3% hydrogen peroxide.

By comparing the factors listed in table 4 to those in table 2, we resolved that ^{212}Pb is much easier to clean than ^{210}Po and ^{210}Pb. Several factor can justify this difference: First, the ^{210}Po-loading of the samples took some years whereas the ^{212}Pb-loading only lasted some days. The longer

the samples were exposed to radon, the deeper it could diffuse inside the samples. Moreover, the different half-lives of the radon isotopes involved in the loading would also play an important. ^{220}Rn decays in the range of seconds ($\tau_{Rn220} = 56$ s), whereas ^{222}Rn has a half-life of 3.6 days. As a noble gas, radon barely interacts with any molecule so it carries out most of the diffusion. The longer it takes before it decays, the deeper it can diffuse inside the PTFE. Indeed, from the shape analysis outlined in section 4.6, we concluded that the alphas were emitted by ^{210}Po from a deeper layer of the bulk than those emitted by ^{212}Bi. Thus, the diffusion effects had been more significant in the former.

5 Summary and outlook

The radioactive noble gas ^{222}Rn is the main source of background in the XENON1T dark matter experiment. One reason is the plate out of radon daughters onto the surface of detector materials, such as PTFE. Subsequent decays of these isotopes can mimic dark matter signals due to limited position reconstruction and partial signal loss at the detector's wall. Therefore, minimizing this background source is crucial to improve the sensitivity of upcoming experiments. In this thesis we investigated different cleaning procedures for their capability to remove radon daughters from PTFE surfaces.

In order to measure the activity of radon daughters on PTFE samples two alpha spectrometers were employed. Their main component is a silicon PIN diode. Radon daughters emit alpha-particles from the surface of the PTFE samples which reach the diode. The detection efficiency of both spectrometers were determined by means of Monte Carlo simulations, finding efficiency factors of 0.136 ± 0.002 and 0.151 ± 0.002, respectively. The detector response was calibrated and was found to be linear with the emitted alpha energies in the region of interest. The background of the detectors due to long lived radon daughters implanted into the diodes in previous measurements was quantified and regularly monitored.

In chapter 3 we studied the removal of ^{210}Po from PTFE samples which had been exposed to radon enriched air for several years. Different standard cleaning procedures were tested such as ethanol wiping, ethanol immersion and other procedures based on HNO_3. The latter consisted on immersion and sonication of the PTFE samples in nitric acid followed by rinsing with de-ionized water and drying by means of nitrogen blowing. Thereby we studied also the effects of different acid concentrations, temperatures or duration of the cleaning baths.

The effect of the cleaning procedures was quantified by measuring the ^{210}Po reduction on the sample's surface. The determined reduction factors are gathered in table 2. Typically a ^{210}Po reduction by a factor of two was found after several cleaning steps.

In addition, the removal efficiency of ^{210}Pb was probed. Since the employed spectrometers cannot measure low energetic beta decays, the cleaning of ^{210}Pb was inferred from the evolution of the ^{210}Po activity over months. The obtained reduction factors were similar to those of ^{210}Po.

In chapter 4, we shifted our focus to the plate out of ^{220}Rn daughters. The short half-lives within the ^{220}Rn decay chain facilitates the study of ^{212}Pb removal more directly with respect to ^{210}Pb where an activity monitoring over months is necessary. In the case of ^{212}Pb, the activity can be determined via its daughter isotopes ^{212}Bi and ^{212}Po which undergo alpha-decays. Further PTFE samples were loaded with ^{220}Rn daughters in a dedicated setup. For a direct comparison, the same cleaning procedures as tested for ^{210}Po removal were investigated. But also new procedures have been tested, for instance one based on acetic acid and a mixture of HNO_3 and H_2O_2.

Two complimentary methods were used to analyze the ^{212}Pb reduction factors. Those were noticeably greater than obtained for ^{210}Po and ^{210}Pb as can be seen from comparing tables 4 and

2. The so-called weak HNO_3 procedure achieved a reduction factor of 5.2 ± 0.3, while the so-called strong HNO_3 procedure achieved a reduction larger than 25.

An explanation for the more efficient removal of ^{212}Pb compared to ^{210}Pb was found when analyzing the peak shapes of the subsequent alpha decays of ^{212}Bi and ^{210}Po, respectively. In case of ^{210}Po the larger tailing towards lower energies indicates that the ^{222}Rn daughters had reached deeper layers underneath the surface. This might be caused by diffusion over long time enabled by the long half-life of ^{210}Pb. Since the cleaning procedures effect only the radon daughters at the surface, the removal was more efficient in case of ^{212}Pb.

This study provides guidelines on how to treat PTFE surfaces for radon-daughters removal. Several cleaning agents have been tested and their capability has been investigated. These procedures, however, might have side effects. The chemicals used might cause outgassing from the PTFE and compromise the purity the xenon target in the detector. Mass spectroscopy can be carried out to examine the outgassing composition of a sample after being treated. Together with a double-phase xenon TPC to imitate the conditions of the XENON detectors, the effective impact of the outgassing of PTFE could be quantified.

List of Figures

List of Tables

References

[1] Y. Akrami et al. Planck 2018 results. I. Overview and the cosmological legacy of Planck. 2018.

[2] Fritz Zwicky. The redshift of extragalactic nebulae. *Helv. Phys. Acta*, 6:110, 1933.

[3] Vera C. Rubin and W. Kent Ford, Jr. Rotation of the Andromeda Nebula from a Spectroscopic Survey of Emission Regions. *Astrophys. J.*, 159:379–403, 1970.

[4] Yoshiaki Sofue and Vera Rubin. Rotation curves of spiral galaxies. *Ann. Rev. Astron. Astrophys.*, 39:137–174, 2001.

[5] Douglas Clowe, Maruša Bradač, Anthony H Gonzalez, Markevitch, et al. A direct empirical proof of the existence of dark matter. *The Astrophysical Journal Letters*, 648(2):L109, 2006.

[6] Matthias Bartelmann and Peter Schneider. Weak gravitational lensing. *Physics Reports*, 340(4-5):291–472, 2001.

[7] Maxim Markevitch et al. Direct constraints on the dark matter self-interaction cross section from the merging galaxy cluster 1e 0657–56. *The Astrophysical Journal*, 606(2):819, 2004.

[8] Volker Springel, Carlos S Frenk, and Simon DM White. The large-scale structure of the universe. *Nature*, 440(7088):1137, 2006.

[9] J. L. Feng. Dark matter candidates from particle physics and methods of detection. *Annual Review of Astronomy and Astrophysics*, 48:495–545, 2010.

[10] Teresa Marrodán Undagoitia and Ludwig Rauch. Dark matter direct-detection experiments. *Journal of Physics G: Nuclear and Particle Physics*, 43(1):013001, 2015.

[11] Cristiano Alpigiani. Searches for dark matter in atlas. *arXiv preprint arXiv:1708.09674*, 2017.

[12] Adish Vartak. Dark matter search in CMS. In *Proceedings, 52nd Rencontres de Moriond on Very High Energy Phenomena in the Universe: La Thuile, Italy, March 18-25, 2017*, pages 225–233, Geneva, 2017. CERN, CERN.

[13] MG Aartsen et al. Search for neutrinos from decaying dark matter with IceCube. *arXiv preprint arXiv:1804.03848*, 2018.

[14] Lucia Rinchiuso, Emmanuel Moulin, et al. Dark matter searches toward the galactic centre halo with HESS. *arXiv preprint arXiv:1711.08634*, 2017.

[15] O Adriani et al. Observation of an anomalous positron abundance in the cosmic radiation. *arXiv preprint arXiv:0810.4995*, 2008.

[16] Mark W. Goodman and Edward Witten. Detectability of certain dark-matter candidates. *Phys. Rev. D*, 31:3059–3063, Jun 1985.

[17] JI Read. The local dark matter density. *Journal of Physics G: Nuclear and Particle Physics*, 41(6):063101, 2014.

[18] Anne M. Green. Astrophysical uncertainties on direct detection experiments. *Modern Physics Letters A*, 27(03):1230004, 2012.

[19] J Billard, E Figueroa-Feliciano, and L Strigari. Implication of neutrino backgrounds on the reach of next generation dark matter direct detection experiments. *Physical Review D*, 89(2):023524, 2014.

[20] Aprile E. and others (XENON collaboration). Dark Matter Search Results from a One Ton-Year Exposure of XENON1T. *Phys. Rev. Lett.*, 121(11):111302, 2018.

[21] DS Akerib et al. Results from a search for dark matter in the complete LUX exposure. *Physical review letters*, 118(2):021303, 2017.

[22] Andi Tan et al. Dark Matter Results from First 98.7 Days of Data from the PandaX-II Experiment. *Phys. Rev. Lett.*, 117(12):121303, 2016.

[23] F Petricca, G Angloher, P Bauer, A Bento, C Bucci, L Canonica, X Defay, A Erb, F v Feilitzsch, N Ferreiro Iachellini, et al. First results on low-mass dark matter from the CRESST-iii experiment. *arXiv preprint arXiv:1711.07692*, 2017.

[24] SuperCDMS Collaboration et al. WIMP-search results from the second CDMSlite run. *Phys. Rev. Lett*, 116, 2016.

[25] Laboratori Nazionali del Gran Sasso. https://www.lngs.infn.it/en/lngs-overview. Accessed: 2018-10-20.

[26] Aprile E. and others (XENON collaboration). First results from the XENON10 dark matter experiment at the gran sasso national laboratory. *Physical Review Letters*, 100(2):021303, 2008.

[27] Aprile E. and others (XENON collaboration). Dark matter results from 225 live days of XENON100 data. *Physical review letters*, 109(18):181301, 2012.

[28] XENON collaboration. Private communication.

[29] Aprile E. and T Doke. Liquid xenon detectors for particle physics and astrophysics. *Reviews of Modern Physics*, 82(3):2053, 2010.

[30] XENON collaboration. private communication.

[31] Aprile E. and others (XENON collaboration). Physics reach of the XENON1t dark matter experiment. *Journal of Cosmology and Astroparticle Physics*, 2016(04):027, 2016.

[32] Palladino KJ Cooley, J et al. Input comparison of radiogenic neutron estimates for ultra-low background experiments. *Nuclear Instruments and Methods in Physics Research Section A: Accelerators, Spectrometers, Detectors and Associated Equipment*, 888:110–118, 2018.

[33] Aprile E. and others (XENON collaboration). Conceptual design and simulation of a water cherenkov muon veto for the XENON1T experiment. *Journal of instrumentation*, 9(11):P11006, 2014.

[34] Diego Ramrez Garca. Monte carlo simulations of a neutron veto for the XENONnT dark matter experiment. Master's thesis, University of Mainz, 2017.

[35] Aprile E. and others (XENON collaboration). Material radioassay and selection for the XENON1T dark matter experiment. *Eur. Phys. J.*, C77(12):890, 2017.

[36] G. Heusser et al. Giove: a new detector setup for high sensitivity germanium spectroscopy at shallow depth. *The European Physical Journal C*, 75(11):531, 2015.

[37] S Rosendahl et al. A cryogenic distillation column for the XENON1T experiment. *Journal of Physics: Conference Series*, 564(1):012006, 2014.

[38] G Keller, B Hoffmann, and Th Feigenspan. Radon permeability and radon exhalation of building materials. *Science of the total environment*, 272(1-3):85–89, 2001.

[39] MM Bé, V Chisté, et al. Table of radionuclides (vol. 4–a= 133 to 252). *BIPM, Sevres*, 2008.

[40] Stefan Augustin Brünner. Study of radon adsorption on activated carbon for a purification system in XENON1T. Diploma Thesis, Karl-Franzens-Universtitt, Graz, 2013.

[41] Triboelectric series. https://www.alphalabinc.com/triboelectric-series/. Accessed: 2018-10-21.

[42] P. Pagelkopf and J. Porstendörfer. Neutralisation rate and the fraction of the positive ^{218}Po-clusters in air. *Atmospheric Environment*, 37:1057–1064, 2003.

[43] Stefan Augustin Brünner. *Mitigation of 222Rn induced background in the XENON1T dark matter experiment.* PhD thesis, University of Heidelberg, 2017.

[44] Natascha Rupp. On the detection of 222rn with minaturized proportional counters: background, sensitivity studies of and results for XENON1T. Master's thesis, University of Heidelberg, 2015.

[45] F. Joerg. Investigation of coating-based radon barriers and studies towards their applicability in liquid xenon detectors. Master's thesis, University of Heidelberg, 2017.

[46] Simgen H. et al. Detection of 133xe from the fukushima nuclear power plant in the upper troposphere above germany. *Journal of environmental radioactivity*, 132:94–99, 2014.

[47] Aprile E. and others (XENON collaboration). Online rn-222 removal by cryogenic distillation in the XENON100 experiment. *The European Physical Journal C*, 77(6):358, 2017.

[48] J. Kiko. Detector for ^{222}Rn measurements in air at the 1 mBq/m ^{3} level. *Nuclear Instruments and Methods in Physics Research A*, 460:272–277, March 2001.

[49] T. Skwarnicki. *A study of the radiative CASCADE transitions between the Upsilon-Prime and Upsilon resonances*. PhD thesis, Cracow, INP, 1986.

[50] S. Pommé, L. Johansson, G. Sibbens, and B. Denecke. An algorithm for the solid angle calculation applied in alpha-particle counting. *Nuclear Instruments and Methods in Physics Research A*, 505:286–289, June 2003.

[51] John T. Conway. Calculations for a disk source and a general detector using a radiation vector potential. *Nuclear Instruments and Methods in Physics Research Section A-accelerators Spectrometers Detectors and Associated Equipment - Nucl Instrum Meth Phys Res A*, 589:20–33, 04 2008.

[52] L. Ruby. Further comments on the geometrical efficiency of a parallel-disk source and detector system. *Nuclear Instruments and Methods in Physics Research Section A: Accelerators, Spectrometers, Detectors and Associated Equipment*, 337(2-3):531–533, 1994.

[53] B. Gonzalez Prieto et al. Equilibrium evaporation of trace polonium from liquid leadbismuth eutectic at high temperature. *Journal of Nuclear Materials*, 450(1):299 – 303, 2014. Special Theme Issue on Spallation Materials Technology. Selected papers from the Eleventh International Workshop on Spallation Materials Technology (IWSMT-11).

[54] Obara T. et al. Polonium evaporation and adhesion experiments for the development of polonium filter in leadbismuth cooled reactors. *Progress in Nuclear Energy*, 50(2):556 – 559, 2008. Innovative Nuclear Energy Systems for Sustainable Development of the World. Proceedings of the Second COE-INES International Symposium, INES-2, November 26-30, 2006, Yokohama, Japan.

[55] G. Zuzel, K. Pelczar, and M. Wjcik. Removal of 222rn daughters from metal surfaces. *AIP Conference Proceedings*, 1921(1):070004, 2018.

[56] N. Hara. The dissolving mechanisms of cadmium and lead in nitric acid. *Industrial Health*, 5(1):60–64, 1967.

[57] G Schupp et al. Transition intensities in the tl 208 beta decay, the bi 212 po 212 decay scheme, and the bi 212 branching ratio. *Physical Review*, 120(1):189, 1960.

Acknowledgments

I would like to thank Prof. Manfred Lindner for giving me the chance to be part of the XENON group at the Max Planck Institut für Kernphysik, where I worked on this thesis, and for the conferences and talks I could attend at that time. Many thanks to Prof. Stephanie Hausmann-Menzemer too for second-refereeing it.

This thesis would not have been possible without the help and supervision of my colleagues at the MPIK. Particularly indispensable was the help and guidance of Stefan Brnner, who patiently oriented me and helped me solving any problems encountered during this year, and who had to put up with me mis-spelling his surname even in the acknowledgments. I must thank Hardy and Teresa for their valuable advice throughout this time and for the friendly working atmosphere. I would like to thank Guillaume for his socratic method and for constantly putting up with me challenging him and his "English accent". Special thanks to all my other colleagues Florian, Natascha and Dominick who had time for me even in Walpurgisnacht; Veronica, Constanze, Oliver and Luisa. I must also acknowledge Jonas and Steffen for their immediate help when anything needed to be repaired (even my keyboard), and Alice and Judith for their support and warm company in the lab.

As Guillaume once told me "*you have too many friends*", so they must be included here too. Thanks to Pau, Víctor for the unspeakable support during the year and the writing phase and for many dinners. Thanks to José, Helena and Cristian for the inspiration and the many laughs (and the salt). Thanks to Marco Hornung and Jack Wilson for forcing me to go for a run every now and then, to Nila for putting up with me explaining her what gadolinium is at 3 a.m and to Román, for showing me that *Dark lives Matter*. Thanks as well to the Mexican, Italian and Kiwi crews, you know I love you guys, but you are just *too many*.

Last but not least, I thank my parents Jesús and Concha, for gauging with incredible precision when I needed to be pushed forward and when I needed to let go a bit. Thanks to my brother Jesús and my cousin Jorge for patiently listen and even encouraging me to keep talking about my "crazy physicist stuff" during their visit to the Insititute.

Oh! And, of course, I want to thank Stefan again for his personal financing of the project with my so-called "salary". Did you think I'd forget that?

Erklärung:

Ich versichere, dass ich diese Arbeit selbstständig verfasst habe und keine anderen als die angegebenen Quellen und Hilfsmittel benutzt habe.

Heidelberg, den 29.10.2018 .....